https://doi.org/10.5194/egusphere-2023-2646
Preprint. Discussion started: 13 November 2023

Diverse mixing state and ice nucleation properties of aerosol particles over the Western Pacific and the Southern Ocean

Jiao Xue[1], Tian Zhang[1], Keyhong Park[2], Jinpei Yan[3], Young Jun Yoon[2], Jiyeon Park[2,*], Bingbing Wang[1,4,*]

[1] State Key Laboratory of Marine Environmental Science, College of Ocean and Earth Sciences, Xiamen University, Xiamen, 361102 China

[2] Korea Polar Research Institute, Incheon, 21990 South Korea

[3] Third Institute of Oceanography, Ministry of Natural Resources, Xiamen 361005, China

[4] Center for Marine Meteorology and Climate Change, Xiamen University, Xiamen, 361102 China

*Correspondence: Bingbing Wang (Bingbing.Wang@xmu.edu.cn) and Jiyeon Park (jypark@kopri.re.kr).

https://doi.org/10.5194/egusphere-2023-2646
Preprint. Discussion started: 13 November 2023

Abstract

Atmospheric particles from different sources can impact cloud formation and play a critical role in regulating cloud properties. However, particle characteristics at single particle level and their abilities to serve as ice nucleating particles (INPs) over different marine atmosphere are poorly understood. Here, we present characterizations and ice nucleation properties of particles collected during a northern and southern hemisphere cruise from South Korea to Antarctica. Micro-spectroscopic analysis was used to obtain composition of individual particles and mixing state of particle populations. Major particle classes were identified and have different contributions over the Western Pacific and the Southern Ocean, including fresh and aged sea salt, sea salt mixed with sulfate, carbonaceous, sulfur-containing, and dust particles. Increasing contribution of fresh sea salt particles, the dominate particle class in the samples, tended toward an increasing mixing state index indicating the population becoming more internally mixed. Aging processes and new particle sources introduce particles with new compositions resulting in external mixtures. We found that the investigated particles demonstrated a variety of ice nucleation abilities at cirrus conditions. The identified INPs are all major particle classes present in the population, and the sea salt mixed sulfate particle is enriched in INPs. Aging processes affected both particle mixing state and their ice nucleation abilities. We tested different ice nucleation parameterizations of marine atmospheric particles for their applicability. Finally, we discuss how the mixing state of particle populations impacts ice nucleation in the atmosphere.

Keywords: Ice nucleation, Ice nucleating particles, single particle analysis, marine aerosols, elemental composition, mixing state

https://doi.org/10.5194/egusphere-2023-2646
Preprint. Discussion started: 13 November 2023

1. Introduction

As 70.8% of the Earth's surface is covered by oceans, marine aerosol particles are one of the most important types of natural aerosols in the global inventory (Myriokefalitakis et al., 2010; de Leeuw et al., 2011). Aerosols in marine environments can not only affect the ocean biogeochemical cycles, but also indirectly or directly affect the radiation budget of the Earth system (Song et al., 2022). The sixth intergovernmental panel on climate change assessment report stated that there is the large uncertainty in the net effective radiative forcing of aerosol in which the aerosol-cloud interactions contribute the most (Masson-Delmotte et al., 2021). The impacts of atmospheric particles on cloud microphysical processes is still poorly understood (Stocker et al., 2013). The physicochemical properties of particles determine their abilities to serve as cloud condensation nuclei and ice nucleating particles (INPs), thereby affecting cloud microphysical processes. Particles serving as INPs can potentially trigger ice nucleation via four pathways: (1) deposition ice nucleation (DIN), which is a direct deposition of gaseous water vapor to a particle's surface forming ice; (2) immersion freezing (IMF), which is freezing of droplets triggered by immersed particles; (3) contact freezing, when droplets freeze by contact with particles; (4) condensation freezing, when droplets freeze as water vapor condenses on droplets or particles. The majority of recent studies focus on the IMF and DIN at mixed-phase and ice cloud conditions (Hoose and Möhler, 2012; Murray et al., 2012; Kanji et al., 2017; Knopf et al., 2018).

There is a diversity of sources and atmospheric processes that bring great challenges to study the physicochemical properties of marine particles. One major particle type in marine atmosphere are sea spay aerosol (SSA) particles generated from waving breaking and bubble bursting over the ocean surface. Their compositions are mainly affected by seawater, sea ice, and biological activities and have minimum influences by anthropogenic activities (Kunwar et al., 2023). Other sources may also contribute including ship emission (Ault et al., 2009, 2010) and terrestrial transport by wind-driven such as industrial emission, biomass burning, dust storm, and fossil fuel combustion

https://doi.org/10.5194/egusphere-2023-2646
Preprint. Discussion started: 13 November 2023

(Han et al., 2006; Fu et al., 2013; Geng et al., 2019). Additionally, atmospheric oxidation of volatile organic compounds from the ocean or anthropogenic activities results in the gas-particle conversion and forming secondary particles (Cochran et al., 2017). For example, dimethyl sulfide (DMS) from marine source is oxidized to form methanesulfonic acid (MSA) and sulfuric acid (H_2SO_4) in the atmosphere (Barnes et al., 2006; Chen et al., 2018; Berndt et al., 2023). Moreover, multiphase reactions can occur on the surface or within particles causing the changes on the physicochemical properties of particles (Cochran et al., 2017). The oxidation products of DMS, H_2SO_4 and MSA, can react with sea salt particles resulting in chloride depletion from acid displacements (Liu et al., 2011). Mineral dust and anthropogenic pollutants from continents can be transported to oceans and mix with marine background aerosol (Zhou et al., 1990; Sasakawa and Uematsu, 2002; Boreddy and Kawamura, 2015). In our study, we aim address this particle complexity from coastal to remote oceans.

Quantifying chemical mixing state helps us to discuss how the population with different internal or external mixing affect their optical properties, cloud formation properties and thus their climatic impacts (Riemer et al., 2019). Due to the diverse sources and dynamic evolution in the atmosphere, individual particles become mixtures of various compositions and have complex morphology. Chemical mixing state is a term to describe how various chemical species are mixed within individual particles in an aerosol population (Riemer et al., 2019). Particles with different composition and morphology are known to have vastly different efficiencies to nucleate ice. Therefore, it is necessary to study the physical and chemical characteristics of individual particles as well as how they are mixed to quantify the fundamental details of, e.g., cloud microphysical processes (Cziczo et al., 2017; Kanji et al., 2017; Knopf et al., 2018; Riemer et al., 2019; Burrows et al., 2022). Using single-particle techniques, previous studies have focused on mixing states including, but not limited to, marine particles (Ault et al., 2010; Park et al., 2014; Tomlin et al., 2021), biomass burning aerosol (Tomlin et al., 2022; Healy et al., 2013), and dust particles (Fraund et al., 2017; Adachi et al., 2020). A review of previous studies (Riemer et al., 2019) quantified the aerosol

https://doi.org/10.5194/egusphere-2023-2646
Preprint. Discussion started: 13 November 2023

mixing state with an index, χ, based on the mass percentages of various chemical species in single particles within a population. However, there are limited studies focusing on quantifying χ from single particle component information of marine particles.

Laboratory and field work suggest that various particle types have potential impacts on atmospheric ice crystal formation. Natural INPs include mineral dust, soil particles, volcanic ash, sea spray aerosol, biomass burning aerosols, and bioaerosols. Anthropogenic INPs include agricultural particles, metals and metal oxides from industrial processes, and fossil fuel combustion particles (Hoose and Möhler, 2012; Murray et al., 2012; Kanji et al., 2017). For marine related particles, Schill and Tolbert (2014) found that SSA were efficient INPs below 225 K. Wanger et al. (2018) showed that SSA and desert dust particles share the same order of magnitude of ice nucleation active surface site densities. Knopf et al. (2011) confirmed that intact cells or fragments of marine diatom can act as INPs. Wilson et al. (2015) demonstrated that sea surface microlayer enriched ice nucleating materials that may be phytoplankton fragments. McCluskey et al. (2018) identified and found two types of INPs from mesocosm experiments, which were dissolved organic carbon coated particles and particulate organic carbon particles like intact cells or cell fragments from microorganisms. Alpert et al. (2022) confirmed that INPs in the sea spray aerosol were the sea salt with organic matter, which were exudates released from planktonic microorganisms. Inoue et al. (2021) found high INP concentrations under high wave conditions which were related to the release of organic carbon from the ocean. Welti et al. (2020) collected the INP concentration data over the Arctic, Atlantic, Pacific, and Southern Oceans. They found that ship-based INP measurements over oceans were 1 to 2 orders of magnitude lower than continental observations. INP concentrations were lowest in polar regions and highest in the temperate climate ocean (Welti et al., 2020). Most of the existing field investigations focus on the INPs concentrations for IMF over oceans and at relatively warmer temperature mixed-phase cloud conditions (Hoose and Möhler, 2012; Murray et al., 2012; Kanji et al., 2017; Knopf et al., 2018). Recent field studies have used

https://doi.org/10.5194/egusphere-2023-2646
Preprint. Discussion started: 13 November 2023

advanced micro-spectroscopes and mass spectrometry for imaging and characterizing the INPs and ice crystal residues to understand the nature of the INPs (e.g., Cziczo et al., 2017; Knopf et al., 2018). Our study focuses on the chemical composition and morphology of INPs to fill the gap of knowledge of IMF and DIN at lower temperatures under cirrus cloud conditions from ambient particles in marine environments.

We quantified ice formation potential and mixing state of particles over coastal and open oceans using microscopic based ice nucleation instrumentation and computer-controlled scanning electron microscopy with energy dispersive X-ray spectroscopy (CCSEM/EDX), respectively. In the latter, the observed elemental composition was used to derive χ in 29 different marine ambient particle populations extending from the northern to the southern hemisphere. Ice nucleation onset conditions were measured for representative samples. Individual INPs were characterized and compared with the particle population to relate ice nucleation ability with mixing state. Finally, we performed ice nucleation kinetic analysis based on the experimental data to test theory and various approaches important for quantifying ice nucleation and verifying their validly for cloud formation.

2. Experimental methods

2.1 Particle sampling

Aerosol particles were collected by a four-stage cascade impactor (SKC, Inc.) at sample flow of 9 L min^{-1} on board the Korean ice breaker R/V *Araon* from October 31st to December 12nd in 2019. The inlet was located on the third deck of the ship at about 13 m above sea surface level (Park et al., 2020). As shown in Fig. 1, the cruise crossed about 110 degrees of latitudes from the Western Pacific near South Korea (34.93°N) to the Rose Sea in the Southern Ocean (75.12°S). Samples were collected on transmission electron microscopy (TEM) copper grids (Carbon Type-B, Ted Pella, Inc.) for single particle analysis by CCSEM/EDX and silicon wafer chips (Silson, Ltd.) with the hydrophobic coating (Si_3N_4) for ice nucleation experiment following our previous

https://doi.org/10.5194/egusphere-2023-2646
Preprint. Discussion started: 13 November 2023

studies (Wang et al., 2012a, 2016a; Knopf et al., 2014). Particle samples were stored at room temperature in an airtight container with desiccant until analyzed. Particles collected on the fourth stage of the impactor with a 50% collected efficiency at 0.25 μm diameter were used. Meteorological conditions and black carbon concentrations were measured by the onboard weather station and an aethalometer (AE22, Magee Scientific Co., USA), respectively. Any contamination by ship exhaust was avoided following a previous sampling protocol (Park et al., 2020). A total of 29 samples were selected for analysis, and their sampling location and 72 h backward air mass trajectories are shown in Fig. 1. Backward air mass trajectories were computed using the Hybrid Single-Particle Lagrangian Integrated Trajectory (HYSPLIT) model (Stein et al., 2015; Rolph et al., 2017). Detailed sampling information are listed in Table S1 and include the collecting time, location, and the corresponding meteorological data. Along with black carbon concentration, air temperature, relative humidity, pressure, relative wind speed and wind direction are also shown in Fig. S1.

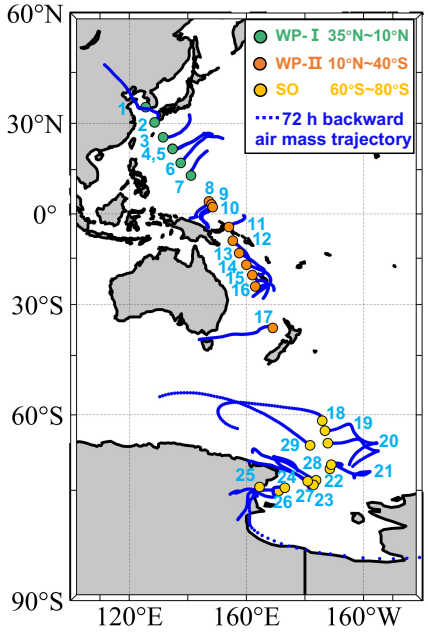

Figure 1. Sampling locations with HYSPLIT 72 h backward air mass trajectories. Solid circles denote the sample locations. Samples were labeled by the numbers. Green, orange, and yellow

https://doi.org/10.5194/egusphere-2023-2646
Preprint. Discussion started: 13 November 2023

circles represent the samples in 35°N – 10°N of Western Pacific (WP-I), 10°N – 40°S of Western Pacific (WP-II), and 60°S – 80°S of Southern Ocean (SO) regions, respectively. Blue lines show the backward trajectories starting from 100 m above sea level.

2.2 Chemical imaging and characterization of particles and INPs

Chemical imaging and single particle analysis to obtain the morphology, size, and elemental composition for the particle population and INPs followed previous works (Laskin et al., 2002, 2006, 2012; Wang et al., 2012a; Knopf et al., 2014; O'Brien et al., 2015) and are briefly introduced here. To characterize the particle population, samples collected on the TEM grids were analyzed using a scanning electron microscopy (Quanta 650, FEI Inc.) equipped with an energy dispersive X-ray spectroscopy (Genesis, EDAX Inc.) in the computer-controlled mode (CCSEM/EDX). CCSEM/EDX operated at 20 kV first detected the particles and determined their sizes. Particle size reported here was the equivalent circle diameter (ECD) based on the two-dimensional projected area of the particle. Particles with size between 0.2 μm and 3 μm were included for analysis in this study. Then, the relative atomic percentages of the selected elements (i.e., elemental composition) for each particle were quantified including C, N, O, Na, Mg, Al, Si, P, S, Cl, K, Ca, Mn, and Fe. We obtained the elemental composition for a significant number of particles, about 630 – 1480 particles for each sample depending the particle loading on the substrates (Table S1). We manually performed SEM/EDX analysis to characterize the individual identified INPs on the silicon wafer chips after ice nucleation experiments described later. In addition, about 10 particles which did not nucleate ice (non-INPs) were randomly selected around each INP for SEM/EDX analysis. X-ray spectra for the INPs and non-INPs were collected at 10 kV. The relative atomic percentages were quantified including elements of C, O, Na, Mg, Al, P, S, Cl, K, and Ca. We excluded N and Si in the quantification since the background substrate contains these two elements.

The relative atomic percentage data were analyzed using a rule-based classification method to assess the contributions of different particle types for each sample (Laskin et

https://doi.org/10.5194/egusphere-2023-2646
Preprint. Discussion started: 13 November 2023

al., 2012; Wang et al., 2012a; China et al., 2018; Lata et al., 2021). According to the classification scheme shown in Fig. 2, particles were grouped into the following seven classes: *i*) "CNO" particles mainly contain C, N, and O elements with traces of other elements. These are carbonaceous particles such as black carbon, secondary or primary organic particles; *ii*) "CNOS" particles mainly contain C, N, O, and S elements with traces of other elements and are sulfates and other sulfur containing particles including their internal mixtures with organics; *iii*) "FreshSS" particles are fresh sea salt particles containing Na above a 2% threshold level of atomic percentage and the ratio of Cl to Na is > 0.8. At the same time, the total atomic percentage of Na, Mg, and Ca, which are dominant cations in sea salt particles, is higher than that of other metals. *iv*) "AgedSS" particles are aged sea salt particles with depletion in Cl, where the ratio of Cl to Na is < 0.8. *v*) "SS/Sulf" particles are aged sea salt particles mixed with sulfur-containing compounds (e.g., sulfate). These particles were mainly composed of Na and S without Cl. *vi*) "Dust"-like particles are from dust storm, road, or soil emissions. These particles have the total atomic percentage of Al and Si above 4% and higher than the total atomic percentage of Na and Mg. *vii*) "Mixture" particles are all remaining particles that did not fit into the classes *i*) – *iv*). The classification scheme was for INPs and non-INPs on silicon wafer chips was altered to account for the Si and N background in the substrate It is important to note that particles on either TEM grids or Si chips were collected at the same time using the same impactor, and therefore the contributions of the respective particle classes for the two are the same. Thus, we modified the classification scheme with this assumption.

https://doi.org/10.5194/egusphere-2023-2646
Preprint. Discussion started: 13 November 2023

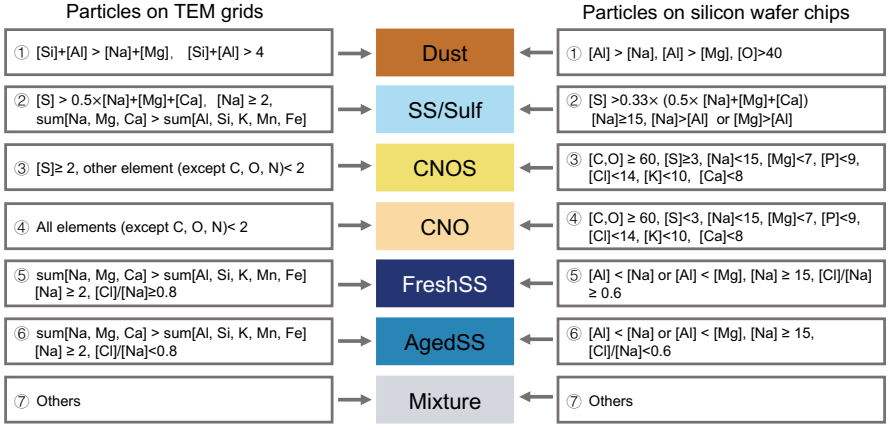

Figure 2. Rule-based particle classification schemes for particles on TEM grids (left) and silicon wafer chips (right). Numbers in the schemes are the relative atomic percentages of corresponding elements or their ratios.

2.3 Chemical mixing state

Chemical mixing state was derived using previous methodology based on mass and entropy metrics (O'Brien et al., 2015; Riemer and West, 2013) and is described briefly here. The particle mass was estimated according to the density and volume of each particle. Particles were assumed to be hemispherical and the volume of each particle was calculated from the equivalent circle diameter obtained by CCSEM. The particle density was assigned according to its classification, with FreshSS, AgedSS, SS/Sulf, CNO, CNOS, Dust, and Mixture particles having a density of 2.0 g/cm^3, 2.0 g/cm^3, 1.7 g/cm^3, 1.3 g/cm^3, 1.3 g/cm^3, 2.7 g/cm^3, and 2.0 g/cm^3, respectively (O'Brien et al., 2015). To calculate the mass of each element in a particle, the atomic percentage of each element obtained by EDX was converted to a weight percentage, then multiplied by the mass of the particle. For the particle i, the mass of element a is equal to:

$$\mu_i^a = \mu_i \left(\frac{elemental\%^a \times molar\ mass^a}{\sum_{a=1}^{A} elemental\%^a \times molar\ mass^a} \right) \quad (1)$$

Where a = 1, …, A (number of elements) and i = 1, …, N (number of particles). a represents elements of Na, Mg, Al, Si, P, S, Cl, K, Ca, Mn, and Fe, and for this list, A =

https://doi.org/10.5194/egusphere-2023-2646
Preprint. Discussion started: 13 November 2023

11. Note that C, N, and O are not included as these three elements are semi-quantitative when EDX analysis is used (Laskin et al., 2006).

First, the total mass of an individual particle, μ_i, the total mass of element a in the particle population (μ^a), and the total mass of the bulk particle population (μ) were calculated using the following equations,

$$\mu_i = \sum_{a=1}^{A} \mu_i^a , \quad (2)$$

$$\mu^a = \sum_{i=1}^{N} \mu_i^a , \quad (3)$$

and

$$\mu = \sum_{i=1}^{N} \mu_i . \quad (4)$$

Then, the mass fraction of element a in the i^{th} particle (p_i^a), the mass fraction of individual particles (p^i) in the particle population, and the mass fraction of element a in bulk particle population (p^a) are

$$p_i^a = \frac{\mu_i^a}{\mu_i}, \quad (5)$$

$$P_i = \frac{\mu_i}{\mu} , \quad (6)$$

and

$$p^a = \frac{\mu^a}{\mu}. \quad (7)$$

Next, the following Shannon entropies (MacKay, 2003) were calculated, where the mixing entropy of the i^{th} particle (H_i) is

$$H_i = \sum_{a=1}^{A} -p_i^a \, lnp_i^a, \quad (8)$$

the average particle mixing entropy (H_a) is

$$H_a = \sum_{i=1}^{N} P_i H_i , \quad (9)$$

and the mass entropy of bulk particle population (H_γ) is

https://doi.org/10.5194/egusphere-2023-2646
Preprint. Discussion started: 13 November 2023

$$H_\gamma = \sum_{a=1}^{A} -P^a lnP^a \,. \quad (10)$$

Shannon entropy is used to describe the mass uniformity of species (elements). High entropy can be regarded as the spread of elements leading to completely uniform in the particle population whereas lower entropy suggests non-uniform mass distribution across the particle population.

Individual particle diversity (D_i) is calculated by taking the exponent of H_i. D_i means the effective number of elements in individual particles, or in other words, indicates the distribution of elements in single particles. D_i ranges from the minimum value of 1 when the particle contains a single element to the maximum value of A when the particle is composed of all A elements with equal mass. Particle elemental diversity (D_α) and bulk population elemental diversity (D_γ) is calculated by taking the exponent of H_a and H_γ, respectively. D_α indicates the average effective number of elements in particles. D_γ indicates the effective number of elements in the whole particle sample. Mixing state index (χ) indicates the homogeneity or heterogeneity of the population and is defined as

$$\chi = \frac{D_\alpha - 1}{D_\gamma - 1} \,. \quad (11)$$

χ ranges from 0% for an externally mixed particle sample with heterogeneous population composing single-component particles ($D_\alpha = 1$) to 100% for internally well mixed particle sample with homogeneous population when all particles have identical compositions.

2.4 Ice nucleation experiment and INP identification

Ice nucleation and water uptake by particles were examined following our previous studies (Knopf et al., 2011, 2014, 2022; Wang and Knopf, 2011; Wang et al., 2012b; Charnawskas et al., 2017; China et al., 2017; Alpert et al., 2022) and are briefly introduced here. Onset conditions of the particle temperature, T_p, and relative humidity with respect to ice (RH_{ice}) when ice nucleation and water uptake occurred were

https://doi.org/10.5194/egusphere-2023-2646
Preprint. Discussion started: 13 November 2023

determined using a custom-built cryo-cooling system. The system consists of a water vapor control component, an ice nucleation cell (INC), and an optical microscopy (OM). Prior to ice nucleation experiments, a particle sample was placed in the INC. Then, a humidified N_2 gas with targeted water vapor partial pressure was continuously introduced into INC at a flow rate of one standard liter per minute. The water partial pressure in the INC was determined by the dew point temperature (T_d) of the gas which was measured using a chilled mirror hygrometer (GE Sensing, Optica). After T_d was stable, T_p was set to about T_d + 3 K and RH_{ice} < 100%. An ice nucleation experiment began and T_p was cooled at a rate of c_r = 0.2 K min^{-1}. Images of particle sample were recorded by OM every 0.02 K. T_d and T_p were recorded every second throughout the experiment. Once ice formation was observed, the sample was slowly warmed to 275 K to sublimate the ice removing any that may be retained in the pores or cavities of particles. Images of ice crystals were acquired during sublimation at high magnification, and the visible particle that served as the INP was identified after complete crystal sublimation. The experiment was repeated 3 – 7 times at similar T_d for reproducibility. Water uptake and ice formation by particles were determined through visual observation and the changes in particle phase or size analyzed by ImageJ software. DIN and IMF were discriminated based on whether particles take up water before ice formation. Only the temperature and RH_{ice} conditions when the first ice crystal formed were reported. RH_{ice} was derived from the measured T_d and T_p (Wang and Knopf, 2011). Particle surface area available for ice nucleation for each sample was estimated from the particle number and size assuming the particles are hemisphere derived from OM and SEM images. The conservatively uncertainty of a factor of 2 for particle surface area was determined and estimated from the standard deviation of the mean and assumption of particles being flat or spherical. This assumption likely underestimates the actual surface area since most of the particles deposited on the substrate exhibited non-spherical geometry and may have had rough surfaces including cracks or cavities. The particle surface areas were later used for ice nucleation kinetic analysis. INPs were identified using the recorded optical images during ice nucleation and ice crystal growth and sublimation. Along with these optical images, INPs were relocated in the SEM

https://doi.org/10.5194/egusphere-2023-2646
Preprint. Discussion started: 13 November 2023

using digital pattern recognition and triangulation and then were imaged and analyzed by SEM/EDX (Knopf et al., 2014).

The temperature and water vapor distribution within the INC were calibrated and validated following our previous work (Wang and Knopf, 2011; Wang et al., 2016b). Homogeneous water vapor distribution in the INC was confirmed by uniform condensation and evaporation of micro-meter size water droplets across the 0.5 mm^2 sample area. T_p was calibrated by the melting points of ice, dodecane, decane, octane, and heptane. The calibration confirmed that the response of T_p is linear in the range of 180 – 273 K with an uncertainty less than 0.3 K. Conservative uncertainty in RH_{ice} for this experimental system comes from the uncertainty in T_d and T_p ($\Delta T_d < \pm 0.15$ K and $\Delta T_p < \pm 0.3$ K) resulting in $\Delta RH_{ice} < \pm 11\%$ at 200 K and $\Delta RH_{ice} < \pm 3\%$ at 260 K.

3. Results and discussion

3.1 Particle characterization

Figure 3 shows the typical SEM images and the corresponding EDX spectra of the identified particle classes. FreshSS and AgedSS particles were dominated by Na with different contents of Cl. The FreshSS particle exhibited the morphology of cubic NaCl crystal (black solid square) with irregular materials (bright coating) under the transmission detector of SEM at darkfield mode. The coating likely composed other materials in seawater including $MgSO_4$ and $CaSO_4$ (Xiao et al., 2008). The AgedSS particle showed a non-cubic shape NaCl crystal as a core surrounded by substances containing Na with depletion of Cl (i.e., Cl/Na < 0.8). The depletion of Cl indicates that the particle had been aged, which may be due to the formation of gaseous HCl by chemical reaction with nitric acid, sulfuric acid, and organic acids in the atmosphere (Laskin et al., 2012; Wang et al., 2015; Angle et al., 2021; Su et al., 2022). The SS/Sulf particle in the Fig. 3 had a core-shell structure and was mainly composed of Na and S without Cl indicating a completely aged sea salt coated with sulfur-containing components, such as sulfate. The CNOS and CNO particles showed a round-shape

https://doi.org/10.5194/egusphere-2023-2646
Preprint. Discussion started: 13 November 2023

morphology. The Dust-like particle exhibited clear Al and Si peaks with minor Ca. Figure 4 shows the particle classification results of more than 30,000 particles in 29 samples investigated by CCSEM/EDX. The size-resolved chemical distributions for all samples are shown in Fig. S2. FreshSS and AgedSS particles dominated all size bins. Majority of SS/Sulf particles were larger than 0.5 μm whereas the CNOS and CNO particles were mainly in sub-micrometer size range. As shown in Fig. 1 and Fig. 4, samples were numbered (S1 – S29) and separated into the following three regions according to the latitudes of sampling locations, 35°N – 10°N of Western Pacific (WP-I), 10°N – 40°S of Western Pacific (WP-II), and 60°S – 80°S of Southern Ocean (SO).

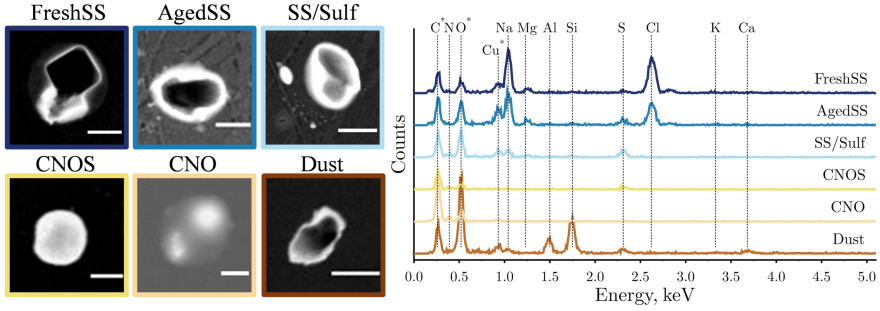

Figure 3. Representative SEM images and the corresponding EDX spectra for particles from each class. The peaks in spectra for the C, O, and Cu elements (asterisked) may include some signal from substrate background of TEM grids. SEM images were captured at 20 kV using scanning transmission electron microscopy detector.

In the WP-I region (35°N – 10°N, S1 – S7), as shown in Fig. 4, the proportions of FreshSS and AgedSS particles both increased as the ship moved away from the land indicating the increased contribution of sea spray aerosol. This is also evidenced as the percentages of FreshSS and AgedSS particles changed from 10% to 91% (Fig. 5A). The contribution of the Dust particle class decreased from 59% to 8% for sample S1 to S3. The Navy Aerosol Analysis and Prediction System reanalysis (NAAPS-RA) product showed that there was a dust storm during the S1 and S2 sampling period (Fig. S3). The 72 h backward air mass trajectories by HYSPLIT also showed that the air mass passed the dust storm areas.

https://doi.org/10.5194/egusphere-2023-2646
Preprint. Discussion started: 13 November 2023

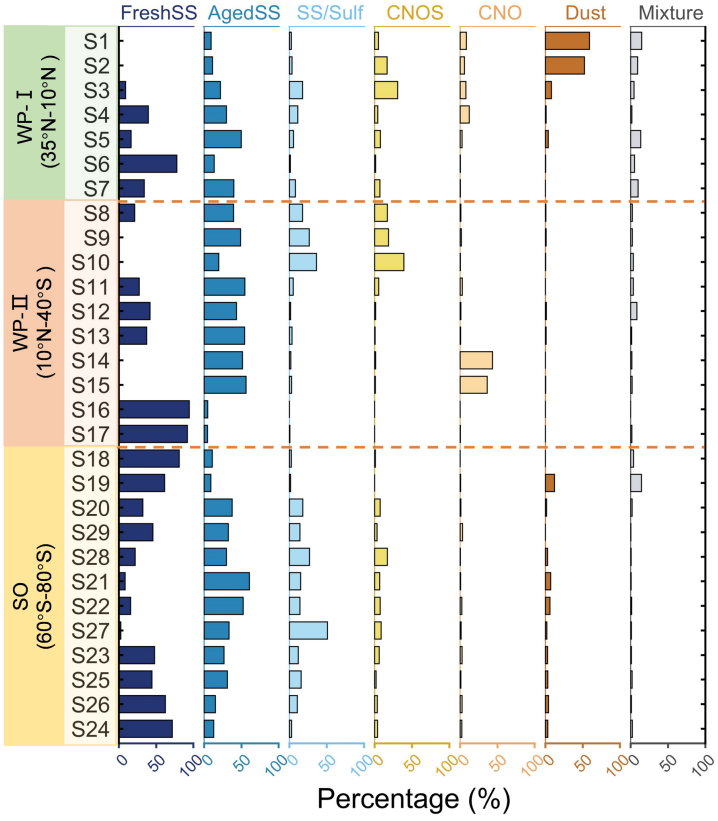

Figure 4. Relative percentages of the seven particle classes (FreshSS, AgedSS, SS/Sulf, CNOS, CNO, Dust, and Mixture) for each sample sorted by the latitudes of sampling locations and separated into three regions (see Fig. 1).

In the WP-II region (10°N – 40°S, S8 – S17), the backward trajectories (Fig. 1) display that the air mass of most samples resided over the ocean. However, the samples demonstrated large variations in the particle composition. S8 – S10 were dominated by AgedSS, SS/Sulf, and CNOS particles, and notably the percentage of SS/Sulf and CNOS particles increased from 18% to 36% and from 17% to 39%, respectively. The contributions of these two sulfur-containing particle classes increased simultaneously implying the same sulfur source. This is consistent with the results showing high sulfate aerosol optical depth (AOD) from the NAAPS-RA products at the same period (Fig. S3D – F). The averaged BC concentration was about 107.4 ± 70.6 ng/m^3 for S8 (Table

https://doi.org/10.5194/egusphere-2023-2646
Preprint. Discussion started: 13 November 2023

S1) and likely from combustion emissions transported from land. This is evidenced by the air mass for S8 came from New Guinea Island, where fires were identified by NASA Fire Information for Resource Management System (FIRMS) seen in Fig. S3C. S14 and S15 were dominated only by the AgedSS and CNO particles, where the latter was 43% and 36%, respectively. These higher fractions of CNO particles as compared to other samples (Fig. 4) are likely related to biomass burning aerosol (BBA). As shown in Fig. S1, the average BC concentrations of S14 and S15 were as high as 674 and 356 ng m^{-3}, respectively. Backward trajectories showed that the air mass passed through the high smoke AOD regions (Fig. S3G – H). These two samples were collected in November 13th and 14th of 2019 which is coincided with the massive wildfires in Australia during the austral summer of 2019 – 2020 (Hirsch and Koren, 2021). Dense fire spots are indicated in Fig. S3I along the east coast of Australia coinciding with the same sampling time. Chemical imaging of elements (Fig. S4) showed that typical CNO particles from these two samples had thick organic coatings with high carbon signal inclusions, and likely are aged BC. This type of aged BBA or smoke particles with organic coatings have been both observed in the stratosphere (Ditas et al., 2018). Similar complex organic compounds also have been observed in the tropospheric smoke aerosol (Palm et al., 2020). The other samples in the WP-II region including S11, S12, S13, S16 and S17 were dominated by FreshSS and AgedSS particles.

In the SO region (60°S – 80°S, sample S18 – S24), the number percentages of FreshSS particles decreased first and then increased as moving toward higher latitude, whereas the AgedSS, SS/Sulf, and CNOS particles had opposite trends. As shown in Fig. S5, the contributions of AgedSS, SS/Sulf, and CNOS type particles to the total from the middle of Rose Sea (S28, S21, S22, S27, S23) were significantly higher than the samples from the north (S18, S19, S20, S29) and southwest (S25, S26, S24) of the Rose Sea. The increased contribution of these three sulfur-containing particle classes may relate to the biogenic sulfur emission from polynyas (an area of open water surrounded by sea ice) in the central Rose Sea. The HYSPLIT 120 h backward trajectories showed some of air masses directly passed over the polynyas (Fig. S6). The formation of polynyas during

https://doi.org/10.5194/egusphere-2023-2646
Preprint. Discussion started: 13 November 2023

the austral summer allowed phytoplankton to grow and produce DMS, which can be transferred into atmosphere and oxidized and thus increase the sulfur content in aerosol particles. Previous works indicated the MSA concentration over the Southern Ocean was about two times higher than that of the western Pacific (Kunwar et al., 2023). High MSA levels were observed in the Ross Sea, which were associated with the dynamic sea ice edge at ~64°S in the early December (Yan et al., 2020). It was caused by the increasing phytoplankton numbers from the algae release of sea ice melting. This also suggests that the potential impacts by the biogenic emission of DMS on these samples.

Figure 5A shows the stacking histogram for the relative number percentages of different particle classes in ambient population. Overall, most of the samples collected during this cruise were predominantly sea salt containing particles with predominant FreshSS, AgedSS, and SS/Sulf classes. The varying proportions of these three particle classes indicated the contribution of marine emission, but with different degrees of aging discussed in the next section. Figure S7A and Fig. S8A show the classification results for super-micron particles (diameter > 1 μm) and submicron particles (diameter between 0.2 and 1 μm), respectively. The sea salt containing particles presented more in the super-micron size range whereas the majority of CNOS particles were in the submicron size range. CNOS represents sulfur containing particles (e.g., sulfate) including their mixtures with organics. CNOS particles mainly existed in submicron particles likely due to new particle formation of MSA and H_2SO_4 and their condensation on pre-exiting particles (Hopkins et al., 2008; Yan et al., 2020; Beck et al., 2021). Heterogeneous aqueous chemical reactions may also contribute to CNOS particles, including cloud processing (e.g., Ervens et al., 2018).

https://doi.org/10.5194/egusphere-2023-2646
Preprint. Discussion started: 13 November 2023

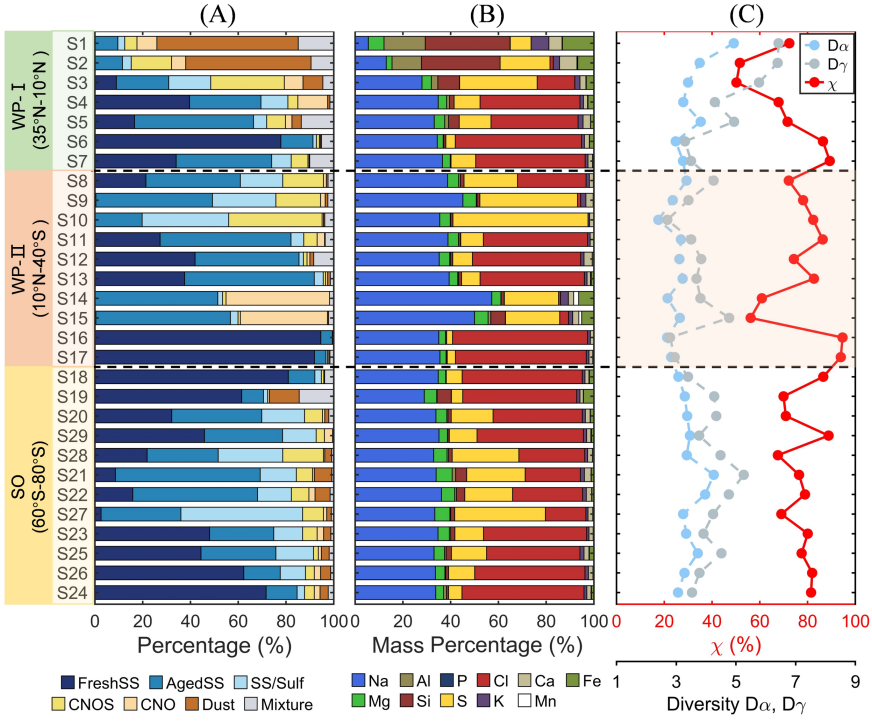

Figure 5. Relative number percentages of different particle class (A), relative mass percentages of elements (B), and mixing state (C) of all samples. Color codes for the particle classes and elements are shown at bottom. Light blue, gray, and red circles represent the particle elemental diversity (D_α), population elemental diversity (D_γ), and mixing state index (χ), respectively.

3.2 Mixing state of particle population

Mixing state described here is based on the elemental composition and referred to chemical mixing state. Figure 5B shows the overall elemental mass percentages of particle population for each sample. Most of the samples were dominated by Na, Cl, and S, except the samples affected by dust storm (S1, S2). The proportion of Na in each sample was relatively stable at about 38%. The rest was contributed mostly by Cl and S. The aging of sea salt particles can be evaluated by the elemental ratio of Cl to Na (Cl/Na). As shown in Fig. 5B and Fig. S9, the values of Cl/Na ranges from 0 to close to 1 indicating complete Cl depletion and no aging on sea salt particles, respectively.

https://doi.org/10.5194/egusphere-2023-2646
Preprint. Discussion started: 13 November 2023

The samples with more S accounted for less Cl which is consistent with the increase in the proportion of sea salt with different aging degrees (AgedSS and SS/Sulf) presented in Fig. 5A. The relationship between S and Cl indicates that the chlorine loss in particles over ocean is attributed to the acid displacement by H_2SO_4 and MSA. The dust storm influenced samples were dominated by the elements of Si, Al, and Fe, all of which were common in mineral dust with trace of Ca and K. As C, N, and O elements were not considered in the mass percentage calculation, the CNO particles prominent in S14 and S15 (Fig. 5A) are not reflected in the mass percentages (Fig. 5B). Elements of K, Si, and Fe presented in the same samples are related to biomass burning (Chen et al., 2017) and is consistent with the air from which they are sampled from impacted by biomass burning plumes.

Figure 5C shows the mixing state parameters, D_α, D_γ, and χ, for each sample. The range of D_α was from 2.4 to 4.9, the range of D_γ was from 2.7 to 6.4 and the range of χ was from 50% to 95%. In the WP-I region, the Dust particles dominated S1 and had the highest D_α of 4.9 and D_γ of 6.4. In other words, there were close to 5 different elements per particle on average and that about 6 were dominant in the bulk aerosol composition. As the contribution of the Dust particles decreased from 59% to 1% for S1 to S4, D_α and D_γ decreased from 4.9 to 3.2 and 6.4 to 4.3, respectively. χ first decreases from 72% to 50% (S1 to S3) and then increases to 68% (S4) as the dominated particles switched to sea salt containing particles. χ increases further to 86% (S6) when the FreshSS particles dominated. In the WP-II region, D_α and D_γ both decreased as CNOS and SS/Sulf particles increased and the mass percentage of S increased from S8 to S10, corresponding to a slight increase in χ from 72% to 82%. When comparing the wildfire influenced samples (S14, S15) and the FreshSS dominated samples (S16, S17), the D_α values are very similar whereas D_γ values are quite different (3.8 and 4.8 vs. 2.8 and 2.9) resulting in contrasting χ values. The highest χ of about 95% for S16 and S17 indicated that these two were largely internally mixed. This can be expected since they were dominated by FreshSS particles from the single marine source. AgedSS particles from marine emission with additional atmospheric processing and CNO particles from

https://doi.org/10.5194/egusphere-2023-2646
Preprint. Discussion started: 13 November 2023

biomass burning had similar contributions to both S14 and S15. This was reflected in χ of about 58% for S14 and S15 and more externally mixed. In the SO region, D_α and D_γ were similar to each other resulting in relatively stable χ values. The changes in D_α and D_γ are mainly due to the changes in the contribution of sulfur-containing particles. Figure S7 and Fig. S8 show the elemental mass percentages, D_α, D_γ, and χ for super-micron and submicron particles, respectively. For submicron particles of each sample, D_α and D_γ are 1.9 – 3.9 and 2.4 – 7.1, respectively. χ ranges from about 38% – 95%. For super-micron particles of each sample, D_α and D_γ are 2.5 – 5.1 and 2.7 – 6.6, respectively. χ ranges from about 54% – 96%. In general, D_α and χ for the submicron particles are lower than super-micron particles for most samples, whereas D_γ is similar. This suggests that super-micron particles tend to be internally mixed more than submicron particles.

Figure 6 shows the relationship between χ and the percentages of FreshSS, Aged SS and SS/Sulf, and CNOS particles. We found a good correlation between the percentages of FreshSS particles in the samples and their χ, especially for submicron particles ($R^2 =$ 0.74). χ increased as the contribution of FreshSS particles increased. We also found a trend that χ decreased as the sum of AgedSS and SS/Sulf particles and the CNOS particles increased. The positive correlation between the contribution of FreshSS particles and χ indicates that the particle population became more internally mixed as more fresh sea spray aerosol particles added into the air parcel. As the FreshSS particles became the dominant type, the particle population was close to the completely internal mixing ($\chi = 100\%$), such as S16 and S17 as discussed above. Here, we show that adding more particles of the dominated particle class (FreshSS) makes the population more internally mixed. Adding CNOS particles (a new particle class) decreases the χ and makes the population more externally mixed. These results verify the schematic description on the evolution of particle mixing state mentioned by Riemer et al. (2019) that adding new types of particles makes the population more externally mixed and adding particles from one dominant particle type makes the population more internally mixed.

https://doi.org/10.5194/egusphere-2023-2646
Preprint. Discussion started: 13 November 2023

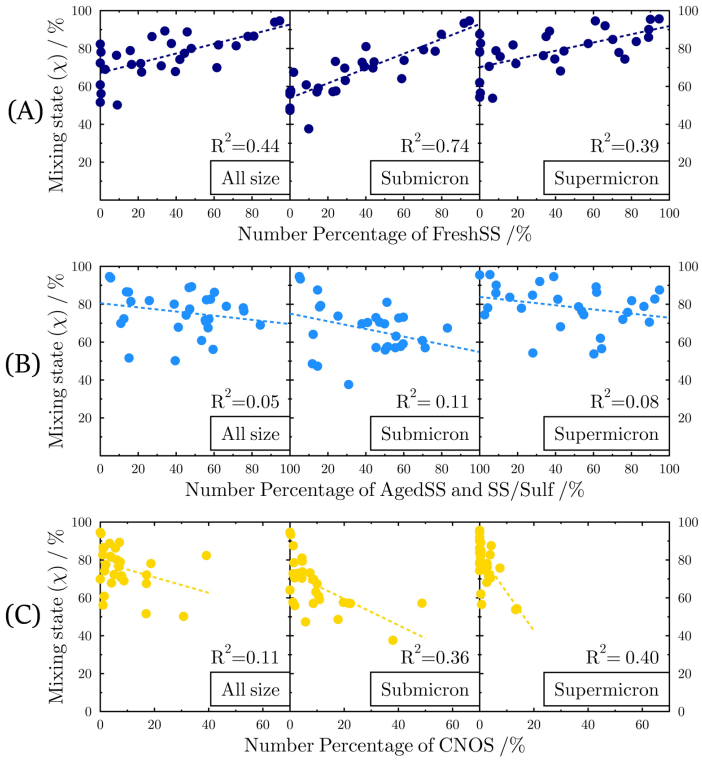

Figure 6. Variation of mixing state index (χ) with the number percentages of different particle classes: (A) FreshSS, (B) AgedSS and SS/Sulf, and (C) CNOS. Panels from left to right are for particles with different size ranges: all particle size (All size), 0.2 − 1 μm (Submicron), and larger than 1 μm in diameter (Super-micron).

The contribution of the AgedSS and SS/Sulf particles can be treated as an indicator for the degree of aging on particle samples, which potentially effects the mixing state. The negative correlation between the number percentages of AgedSS and SS/Sulf particles and χ indicates that aging resulted in a more externally mixed particle population. This seems to be contrary to the view that aging tends a particle population toward a more internally mixed state (Riemer et al., 2019). If an aging process (e.g., condensation of secondary organics) occurs uniformly on each particle, which makes each particle more homogeneous as it is further aged, the population tends to be more internally mixed. On the other hand, if the aging process only occurs on a specific type of particles, such

https://doi.org/10.5194/egusphere-2023-2646
Preprint. Discussion started: 13 November 2023

as acid displacement turning fresh sea salt to aged sea salt, this will increase particle diversity and the population may move to a more externally mixed state. This may especially be true as fresh sea salt will continually be emitted even as aged sea salt particles form. The availability of acids and the size distribution of fresh and aged sea salt particles at different locations could result in particles having different chlorine deficiencies and higher diversity. In this case, aging will increase the inhomogeneity of particles and move the population toward a more externally mixed state.

3.3 Ice nucleation properties at cirrus conditions

We conducted ice nucleation experiments on six samples dominated by different particle classes which are separated into four groups: *i*) Dust dominated sample (S1) accounting for 59% of particles as dust-like. *ii*) BBA influenced sample (S14) that likely had been affected by biomass burning. CNO and AgedSS particles contributed 43% and 51%, respectively. *iii*) CNOS and SS/Sulf dominated sample (S10) with percentages of 39% and 36%, respectively. *iv*) FreshSS and AgedSS dominated samples (S4, S11, and S12) where the total number percentages of the FreshSS and AgedSS particles are 70%, 82% and 85% for S4, S11, and S12, respectively. The dominant particle class, total particle surface area, number of particles available for ice formation during the experiments, IN-activated fraction at ice nucleation onsets, average ECD of INPs and non-INPs, and average ECD of INPs are given in Table 1.

Table 1. Information of particle samples including the total particle surface area and number of particles, IN-activated fraction at ice nucleation onset conditions, the average ECD of INPs and non-INPs, and the average ECD of INPs.

Sample	Dominant particle type	Particle surface area ($\times 10^4$ μm^2)	Particle number ($\times 10^5$)	IN-activated fraction (‰)	ECD for INPs (μm)	ECD for all (μm)
WP-I-S1	Dust	4.35	0.85	0.12 – 0.24	2.53 ± 1.76	1.45 ± 0.98
WP-I-S4	FreshSS+AgedSS	0.54	1.29	0.08 – 0.15	0.99 ± 0.25	0.89 ± 0.25
WP-II-S10	CNOS+SS/Sulf	6.81	9.13	0.01 – 0.03	1.54 ± 0.56	1.21 ± 0.57
WP-II-S11	FreshSS+AgedSS	7.76	6.37	0.02 – 0.03	1.19 ± 0.63	1.03 ± 0.50
WP-II-S12	FreshSS+AgedSS	12.91	8.26	0.01 – 0.02	1.91 ± 1.20	1.22 ± 0.78
WP-II-S14	BBA	13.84	0.56	0.18	5.17 ± 3.12	2.50 ± 2.01

https://doi.org/10.5194/egusphere-2023-2646
Preprint. Discussion started: 13 November 2023

Figure 7 shows the onset conditions of T_p and RH_{ice} for water uptake and ice nucleation on the representative samples. Below 235 K, only DIN was observed for the Dust and BBA samples (Fig. 7A). Particles on the Dust sample nucleated ice heterogeneously at RH_{ice} from 130% ± 9% to 153% ± 8% at T_p from 235 K to 209 K. These values are below the homogeneous nucleation limits of aqueous droplets (Koop et al., 2000; Koop and Zobrist, 2009). RH_{ice} onsets of the BBA sample ranged from 145% ± 5% to 169% ± 1% at T_p from 229 K to 209 K. The RH_{ice} onsets were only about 3% lower than the homogeneous nucleation limits between 228 K to 220 K, and thus samples dominated by BBA may not have been efficient heterogeneous ice nuclei. As T_p decreased, the RH_{ice} onset of both BBA and Dust samples gradually increased. Particles on the Dust sample initiated DIN at RH_{ice} lower than the BBA sample by 7% – 18% at each investigated T_p. For the CNOS and SS/Sulf dominated sample (Fig. 7A), particles first took up water when RH_w reached about 83% and then froze via IMF or homogeneous nucleation with RH_{ice} around the homogeneous line at the temperature close to 230 K. Particles formed ice via DIN below 225 K at RH_{ice} from 136% ± 4% to 159% ± 11%. Figure 7B shows that the ice nucleated on particles from the FreshSS and AgedSS dominated samples through DIN and IMF pathways. The transition temperature between DIN and IMF pathways was about 225 K. At about 225 K, particles on S4 and S12 both took up water at 78% ± 2% and then formed ice with further cooling. The subsequent ice nucleation of S12 could be homogeneous nucleation or IMF since the onset RH_{ice} of 150% ± 7% is close to the homogeneous nucleation limit. However, particles of S4 nucleated ice after water uptake through IMF at RH_{ice} of 140% ± 8% which is about 8% lower than the homogeneous nucleation limit. Below 225 K, particles of S4 and S12 nucleated ice via DIN at RH_{ice} of 133% ± 4% to 170% ± 8%. DIN occurred on the S11 particles at about 121% ± 3% to 130% ± 3% RH_{ice} below 225 K. S11 showed the lowest onset RH_{ice} among the investigated samples indicating that its ice nucleation efficiency was higher than other samples. The results of ice

https://doi.org/10.5194/egusphere-2023-2646
Preprint. Discussion started: 13 November 2023

599 nucleation onset conditions for the investigated samples showed distinct variations in
600 the ice nucleation ability for particles in the different marine atmosphere, even for the
601 samples (S11, S12) with similar elemental composition and the dominated particle
602 classes. The possible reasons will be discussed in the later section.

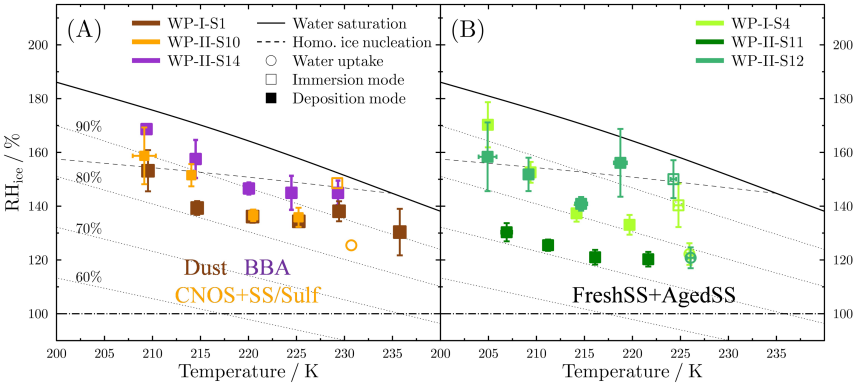

603

604 **Figure 7.** Onset conditions of freezing temperature and RH_{ice} for water uptake (open circles),
605 immersion freezing (open squares), and deposition ice nucleation (solid squares) on particle samples.
606 (**A**) Dust dominated sample (brown), BBA influenced sample (purple), and CNOS and SS/Sulf
607 dominated sample; (B) FreshSS and AgedSS dominated samples. Dashed line indicates the
608 homogeneous freezing limits for aqueous droplets of 0.3 μm in diameter (Koop et al., 2000; Koop
609 and Zobrist, 2009). Dotted lines represent different relative humidity (RH_w) shown in panel A. Solid
610 and dased-dotted lines represent water saturation (100% RH_w) and ice saturation (100% RH_{ice}),
611 respectively.

612

613 **3.4 INP characterization**

614 In total, 132 INPs together with 1317 non-INPs on the Silicon wafer substrates were
615 identified and characterized individually for their morphology and elemental
616 composition. Figure 8 shows the representative SEM images and the corresponding
617 EDX spectra of different types of INPs. SEM images for each identified INP at different
618 temperatures are shown in Fig. S10, Fig. S11, and Fig. S12. The average ECD of INPs
619 was in general greater than the ECD of the population considering both INPs and non-
620 INPs together for each sample (Table 1). Among 132 INPs, 71% of them were super-

https://doi.org/10.5194/egusphere-2023-2646
Preprint. Discussion started: 13 November 2023

micron particles and 29% were submicron particles. The INPs exhibited different morphologies, such as crystalline irregular shapes (e.g., INPs classified as FreshSS, Aged SS, and Dust) and spherical shapes (e.g., INPs classified as CNOS). We found that the majority of INPs from S14 influenced by BBA had thick organic coatings (Fig. 8 and Fig. S10). Among the FreshSS and AgedSS dominated samples, more than 80% of INPs in S11 were coated with organic matter as compared to S4 (33%) and S12 (30%). Figure S13 shows the elemental mapping of a representative INP with thin organic coating. The mapping shows that elements of Na and Cl were distributed in the core and the elements of C and O were distributed over the whole 2-D projected area of this AgedSS INP. Previous studies have shown that the solid organics can form ice via DIN at low temperatures (Wang et al., 2012b; Knopf et al., 2018; Lata et al., 2021; Alpert et al., 2022). We suspect that the organic coatings on the particles of S11 triggered the ice nucleation which have different ice nucleation ability compared with S4 and S12.

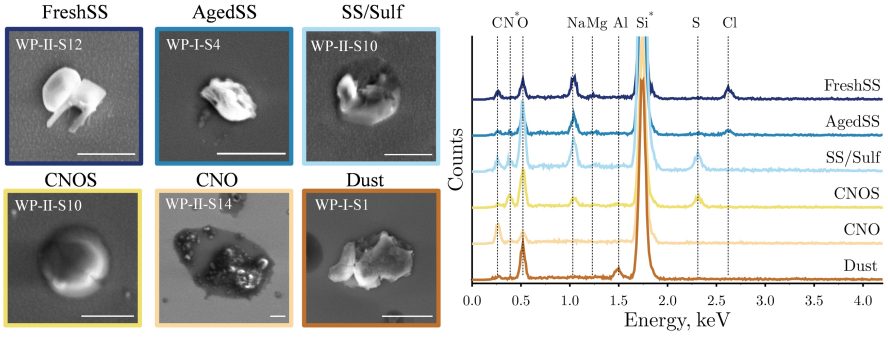

Figure 8. Representative SEM images and the corresponding EDX spectra for 6 classes of INPs. The spectra include the substrate background signal of N and Si (asterisked) from silicon wafer coated with Si_3N_4. Labels on SEM images are the name of samples. Scale bar is 2 μm for all images.

All the identified INPs and non-INPs on the substrates used in the ice nucleation experiments were categorized based on the SEM/EDX data. Figure 9 shows the percentages of different classes for INPs and the particle population in stacked bars marked with “INPs” and “All”, respectively. For each sample, all six particle classes

https://doi.org/10.5194/egusphere-2023-2646
Preprint. Discussion started: 13 November 2023

644 contributed to the particle population for S1 and the 19 identified INPs are from five
645 except the CNO class. Similar to S1, the dominant particle classes in the population of
646 all respective samples are also the dominant classes of INPs. This result suggests that
647 all these major particle classes identified in our experiments are potential INPs. We also
648 found that the contributions of same particle class in the INPs and particle population
649 are different in some cases. The most notable is S10 where SS/Sulf particles were 77%
650 of INPs, but only 51% of the population.

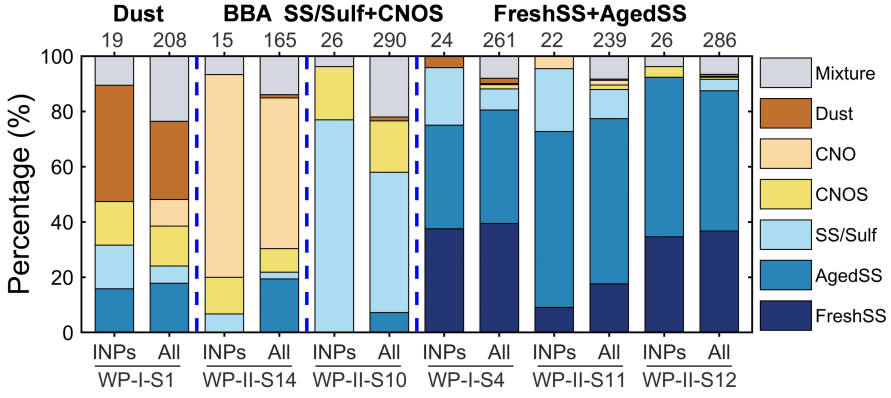

651

652 **Figure 9.** The number percentages of different particle classes for INPs and the particle population.
653 Data marked with "All" including both INPs and non-INPs. The corresponding numbers on the top
654 represent the investigated particle number. Blue dashed lines separate the samples with different
655 particle classes.

656

657 To further explore whether a particle class is unique when acting as INPs, we calculated
658 the enrichment factor (EF) according to the following formula:

659 $$EF_A = \frac{\frac{N_A^{INPs}}{N^{INPs}}}{\frac{N_A^{INPs+nonINPs}}{N^{INPs+nonINPs}}}, \quad (12)$$

660 where A is a certain class of particles and N is the number of particles in that class. EF_A
661 basically is the ratio of the contributions of the particle class A in the INP and the whole
662 particle population. EF > 1.0 and EF < 1.0 means a particle class was enriched or
663 depleted in the INPs, respectively. EF values of each particle class for different samples

https://doi.org/10.5194/egusphere-2023-2646
Preprint. Discussion started: 13 November 2023

664 are shown in Fig. 10. EF values with upper and lower limits determined from Poisson
665 distributed errors at a confidence level of 95% are listed in Table S2. Although the
666 enriched particle classes are diverse for different samples, EF of the SS/Sulf class is
667 larger than 1 for most of the samples except S12. No INP was identified as SS/Sulf
668 particle for S12 which only has 4% of SS/Sulf in the population. The overall EF of
669 SS/Sulf class is 1.9 with the upper and lower limits of 9.2 and 1.2, respectively. This
670 indicates that the SS/Sulf particles were enriched in INPs in these marine environments.

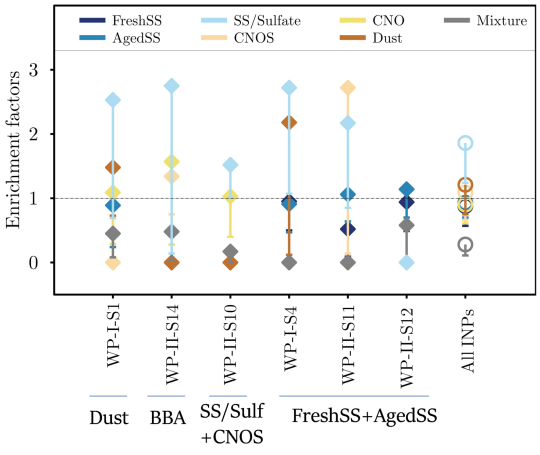

671

672 **Figure 10.** The EFs of all INP classes for each sample (solid diamonds) and all INPs (open circles).
673 The dashed line indicates EF of 1. The lower limits of EFs were calculated by Poisson distribution
674 at the confidence level of 95%. For the readability, the upper limits were not plotted here but the
675 values are listed in Table S2.

676

677 **3.5 Comparison of ice nucleation properties with previous studies**

678 Figure 11 shows the comparison of ice nucleation data from our work and previous
679 studies. The DIN onset conditions of the Dust dominated sample (S1) are similar to the
680 feldspar between 230 K to 235 K (Yakobi-Hancock et al., 2013) and less efficient
681 compared to bare dust particles, including montmorillonite (Welti et al., 2009; Kulkarni
682 et al., 2014), illite (Welti et al., 2009; Kulkarni et al., 2014), quartz (Kulkarni et al.,
683 2014), and kaolinite (Wang and Knopf, 2011). Previous laboratory studies showed that

https://doi.org/10.5194/egusphere-2023-2646
Preprint. Discussion started: 13 November 2023

the aging processes can decrease the ice nucleation ability of mineral dust at temperatures relevant to cirrus clouds (Tang et al., 2016). For example, Primm et al. (2017) pointed out the ice nucleation ability of illite can be slightly suppressed by organic acids when it is mixed with a mixture of five dicarboxylic acids (referred to as M5) at an organic-illite mass ratio greater than 1:1. The DIN onset conditions of S1 are similar to the M5/illite (10:1) mixtures (Fig. 11A). We also found that coated particles (Fig. S14) in S1 are similar in coating thickness and extent as INPs (Fig. S10), also similar to organic coatings on M5/illite greater than 1:1. Kulkarni et al. (2014) observed a decrease in ice nucleation ability of montmorillonite, illite, and quartz at 235 K when coated with H_2SO_4. These H_2SO_4-coated dust particles had a similar onset RH_{ice} with particles on S1 at 235 K. During the cruise, S1 and S2 in the WP-I region were impacted by the dust storm originated from western Asia. The dust particles were aged during the transport to the coastal areas and part of them had clear coatings (Fig. S10 and Fig. S14). This is consistent with the finding by Jang et al.(2023) from the same cruise that in the sample area of S1 aerosol particles have a high fraction of lignin-like organics. S1 had similar ice nucleation ability to dust particles with organic coatings. We suspect that the ice nucleation efficiency of the dust particles at temperatures when DIN occurred at INP's surface was affected by coatings after aging.

Our results for S14 suggest that BBA from the Australian wildfires may have served as INPs via DIN below 230 K. Combustion and burning processes produce a large amount of particles with organic and inorganic mixed components into the atmosphere (e.g., Fuzzi et al., 2007; Chen et al., 2017; Hodshire et al., 2019). Previous studies have shown that soot, combustion ashes, and BBA particles from different burning sources demonstrated various ice nucleation properties (e.g., Jahl et al., 2021; Jahn et al., 2020; Kanji et al., 2017 and references therein). Soot particles or their organic coatings on S14 may have played a role in the observed ice nucleation events. Several studies have reported that combustion related particles can serve as INPs via DIN below 233 K (DeMott et al., 1999; Möhler et al., 2005a, b; Koehler et al., 2009; Kanji et al., 2011; Chou et al., 2013). Kanji et al. (2011) showed the ice nucleation activated by soot

https://doi.org/10.5194/egusphere-2023-2646
Preprint. Discussion started: 13 November 2023

714 generated using Graphite Spark Generator (GSG) at about 145% RH_{ice}, a value similar
715 to S14 at 230 K. Chou et al. (2013) showed that wood burning particles nucleated ice
716 at about 136% RH_{ice} at about 233 K. DeMott et al. (1999) reported the freezing RH_{ice}
717 of soot was close to the homogeneous freezing limits. In comparison to S14 from this
718 study, ice nucleation occurred at lower RH_{ice} than soot generated by GSG and particles
719 with organic carbon (Möhler et al., 2005a, b). Ice nucleation onset conditions of S14
720 are very similar to the Suwannee River standard fulvic acid (SRFA) and ozone aged
721 leonardite particles above 220 K but higher at lower temperatures. SFRA and leonardite
722 were used as surrogates of atmospheric organics from biomass burning (Wang and
723 Knopf, 2011). Thus, it is likely that the organic coating on the particles of S14 has
724 initiated the ice nucleation via DIN at the investigated temperature range.

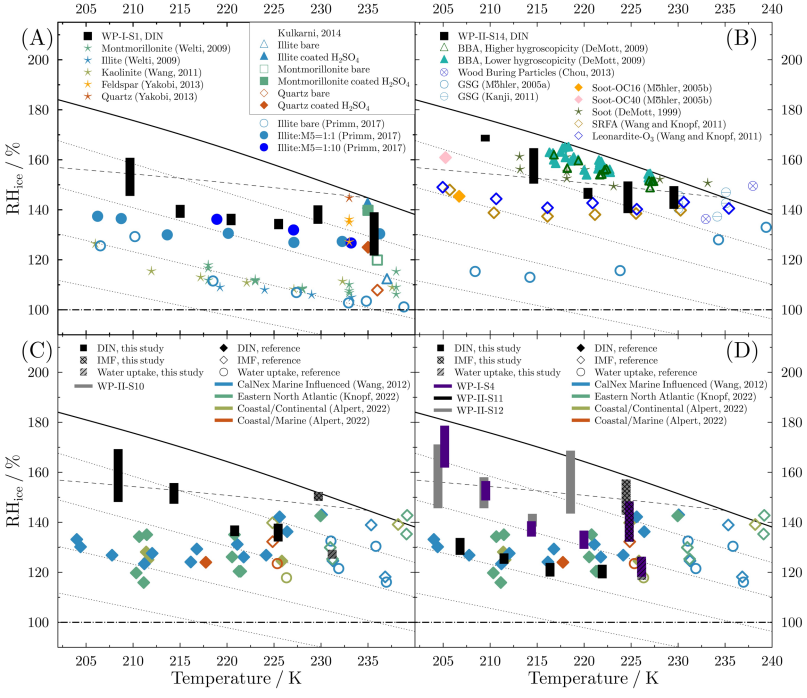

725

726 **Figure 11.** Ice nucleation and water uptake onset conditions (bars) for (A) Dust dominated sample,
727 S1, (B) BBA influenced sample, S14, (C) CNOS and SS/Sulf dominated sample, S10, and (D)
728 FreshSS and AgedSS dominated samples (S4, S11, S12) compared with previous studies (symbols)

https://doi.org/10.5194/egusphere-2023-2646
Preprint. Discussion started: 13 November 2023

(DeMott et al., 1999, 2009; Möhler et al., 2005a, b; Welti et al., 2009; Kanji et al., 2011; Wang and Knopf, 2011; Wang et al., 2012a; Yakobi-Hancock et al., 2013; Kulkarni et al., 2014; Primm et al., 2017; Alpert et al., 2022; Knopf et al., 2022). Descriptions for the lines are the same as in Fig. 7.

Figures 11C and 11D show the comparison of data on marine related particles from previous studies with our data on sea salt containing particles. Several studies have shown that the aerosol particles collected in the marine environments or coastal areas can act as efficient INPs at RH_{ice} between 115% and 143% (e.g., Wang et al., 2012a; Alpert et al., 2022; Knopf et al., 2022). Using the micro-spectroscopic analysis, these studies identified the INPs and demonstrated that the major particle types in the population initiate ice formation. These particle types include the marine influenced particles with thin organic coatings collected during the CalNex field campaign (Wang et al., 2012a), the relatively fresh sea salt particles with marine-produced organics collected from the coast of Long Island, New York (Alpert et al., 2022), and the processed sea salt containing particles collected over the eastern North Atlantic (Knopf et al., 2022). There is one FreshSS and AgedSS dominated sample (S11) that nucleated ice at the same RH_{ice} onsets as compared to those marine-influenced particles from above mentioned studies. The other sea salt containing samples in this work including the CNOS and SS/Sulf dominated sample (S10) and the FreshSS and AgedSS dominated samples (S4, S12) showed very similar RH_{ice} onsets only at temperature above 220 K but higher onsets below 220 K. The reason of this discrepancy at lower temperatures is not clear, but as previously mentioned, we speculate it has something to do with coating thicknesses or coating composition. Together with previous studies, we show these marine-influenced particles display various ice nucleation efficiencies. These variations are likely contributed to not only the complex compositions but also the physical and chemical mixing state of these particles.

3.6 Ice nucleation data analysis

Ice nucleation kinetic analysis was conducted using the experimental data, including the relative humidity and temperature at which ice was observed, along with the

https://doi.org/10.5194/egusphere-2023-2646
Preprint. Discussion started: 13 November 2023

observed surface area, number of nucleation events, and nucleation time. Ice nucleation activated fraction, ice nucleation active sites density (n_s), heterogeneous ice nucleation rate coefficient (J_{het}), contact angle (θ), and their parameterizations are presented and discussed based on the singular hypothesis (SH) and classical nucleation theory (CNT).

3.6.1 Ice nucleation activated fraction

We report the ice nucleation activated fraction as the ratio between the number of particles that nucleated ice to the total particle number available for each ice nucleation experiment (i.e., the number of particles deposited). The numbers of ice crystals determined by OM images is typically one to three ice crystals at the onsets. IN-activated fractions of each sample were summarized in Table 1. It ranges from 0.01‰ to 0.24‰ with the maximum value appeared in S1. It should be noted that the IN-activated fraction determined here should be interpreted as a higher limit at the ice nucleation onset conditions since the number of small particles deposited on the substrate can be underestimated by OM.

3.6.2 Ice nucleation active site density (INAS)

The singular hypothesis (SH) assumes that heterogeneous ice nucleation occurs on active sites located on the particle surface where one active site can form one single ice crystal (Vali, 1971; Connolly et al., 2009). INAS (n_s) is temperature dependent and time independent. Having units of cm^{-2}, n_s is defined as $n_s = N_{ice}/A_{tot}$, where N_{ice} is the number of the observed ice nucleation events that occurred in a temperature interval and A_{tot} is the total particle surface area available for ice nucleation experiment. In this study, the interval of 0.02 K was applied corresponding to the temperature difference between the recorded subsequent OM images. The ensemble of experiments at similar T_d were combined for analysis. Experimentally derived n_s for DIN and IMF as a function of temperature for different types of samples are presented in Fig. 12. n_s demonstrates a strong temperature dependence increasing by about 1 – 2 orders of magnitude as temperature decreases within a few degrees. We provide the exponential fits (solid lines) for n_s as a function of temperature (T), $n_s = 10^{(a \times T + b)}$, at different

https://doi.org/10.5194/egusphere-2023-2646
Preprint. Discussion started: 13 November 2023

temperature ranges. Values of a and b are listed in Table S3. Compared with the other samples, the a (negative value) is larger for the FreshSS and AgedSS dominated samples indicating a weaker dependence of n_s on temperature (Fig. 12). Figure S15 shows the median n_s with 25th and 75th percentiles for all types of samples. For DIN, the Dust dominated sample demonstrated the highest median n_s of about 2×10^3 cm^{-2} whereas the BBA influenced sample had the lowest median n_s of about about 5×10^2 cm^{-2}. This suggests that particles of the Dust-dominated sample are more efficient INPs than the particles of the BBA influenced sample.

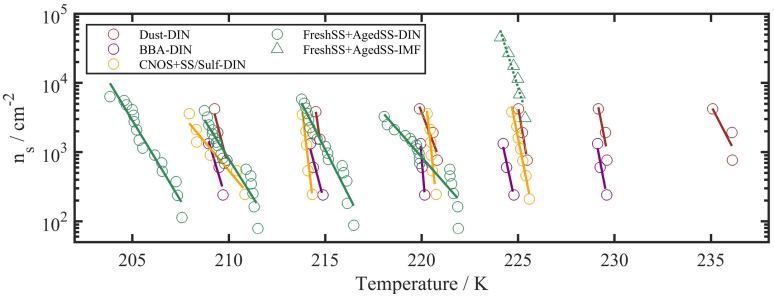

Figure 12. The n_s of all types of samples. Circles and triangles represent DIN and IMF, respectively. Lines indicate the fittings according to $log_{10}(n_s) = a \times T + b$.

3.6.3 Heterogeneous ice nucleation rate coefficient (J_{het})

According to CNT, ice nucleation is a stochastic process and continues with time, in contrast to the singular hypothesis (Pruppacher and Klett, 2010). J_{het} depends on temperature and RH_{ice}. J_{het} was derived following the approach in previous works (Wang and Knopf, 2011; Wang et al., 2012a; China et al., 2017; Knopf et al., 2022) and has units of cm^{-2} s^{-1}. Using observed ice nucleation data, $J_{het} = N_{ice}/(t \times A_{tot})$, where N_{ice} is the number of the observed ice nucleation events occurred in a temperature interval, A_{tot} is the total particle surface area available for ice nucleation experiment in the temperature interval, t of 6 seconds is the time interval between two subsequent OM images used to monitor ice formation.

In the four groups of particle samples we investigated, J_{het} for DIN ranged from 130 to 1370 cm^{-2}, 40 to 2970 cm^{-2}, 40 to 1480 cm^{-2}, and 10 to 390 cm^{-2} for the Dust dominated,

https://doi.org/10.5194/egusphere-2023-2646
Preprint. Discussion started: 13 November 2023

BBA influenced, CNOS and SS/Sulf dominated, and FreshSS and AgedSS dominated samples, respectively. J_{het} for IMF ranged from 540 to 4780 cm^{-2} for the FreshSS and AgedSS dominated samples. The uncertainty of J_{het} has contributions from stochastic freezing (statistical uncertainty) or the number of ice nucleation events, and the uncertainty in temperature, RH_{ice}, and surface area. We followed the method by Alpert and Knopf and quantified the total uncertainty of J_{het} in the form of $\Delta J_{het} = J_{het}\,{}^{\times k}_{\div j}$, indicating the upper and lower limits of a factor k times higher or j times lower (Alpert and Knopf, 2016; China et al., 2017). Statical uncertainty for the Dust, BBA, CNOS and SS/Sulf, and the FreshSS and AgedSS dominated samples were $J_{het}\,{}^{\times 39}_{\div 6}$, $J_{het}\,{}^{\times 48}_{\div 6}$, $J_{het}\,{}^{\times 22}_{\div 5}$, and $J_{het}\,{}^{\times 7}_{\div 3}$, respectively. ΔJ_{het} for IMF of FreshSS and AgedSS dominated samples were $J_{het}\,{}^{\times 61}_{\div 6}$. ΔJ_{het} from a temperature uncertainty of ± 0.3 K were $J_{het}\,{}^{\times 2}_{\div 2}$. ΔJ_{het} from the maximum RH_{ice} uncertainty of ± 11% were $J_{het}\,{}^{\times 10^{0.11c}}_{\div 10^{0.11c}}$, where c is one of the parameters for J_{het} parameterizations in the following discussion. If considering the uncertainty of about a factor of 2 in surface area, ΔJ_{het} was $J_{het}\,{}^{\times 2}_{\div 2}$. Combining all the uncertainties, the DIN ΔJ_{het} of the Dust, BBA, CNOS and SS/Sulf, FreshSS and AgedSS dominated samples were $J_{het}\,{}^{\times 45}_{\div 12}$, $J_{het}\,{}^{\times 55}_{\div 13}$, $J_{het}\,{}^{\times 28}_{\div 11}$, and $J_{het}\,{}^{\times 13}_{\div 9}$, respectively. The IMF ΔJ_{het} of the FreshSS and AgedSS dominated samples was $J_{het}\,{}^{\times 297}_{\div 17}$.

3.6.4 Parameterizations of J_{het} and contact angle

The experimental derived J_{het} were parameterized using two methods, the first based on the water-activity-based approach. The water-activity-based approach has been widely used to describe the homogeneous ice nucleation of droplets and depends only on a droplet's water activity (a_w) and T_p (Koop et al., 2000). Homogeneous ice nucleation temperature follows a single curve as a function of a_w and parameterized with a constant shift of a_w (i.e., Δa_w) from the ice melting temperature curve (Koop and Zobrist, 2009). This approach has also been applied to heterogeneous ice nucleation including DIN and IMF (Koop and Zobrist, 2009; Knopf and Alpert, 2013; China et al., 2017). It is assumed that particles were in equilibrium with the gas phase during the experiments, so $a_w = RH_w/100$. For each nucleation event, $\Delta a_w(T_f)$ is the difference

https://doi.org/10.5194/egusphere-2023-2646
Preprint. Discussion started: 13 November 2023

between the RH_w at which ice nucleated and the RH_w on the ice melting curve at the observed ice nucleation temperature (T_f), or $a_w(T_f)$ and ($a_w^{ice}(T_f)$), respectively. Then, $\Delta a_w(T_f) = a_w^{ice}(T_f) - a_w(T_f)$ (Knopf and Alpert, 2013; Koop and Zobrist, 2009), which can be calculated for each ice nucleation event using the ice nucleation onset temperature and RH. J_{het} was calculated for all ice nucleation events and parameterized as a function of Δa_w following the previous works (China et al., 2017; Alpert et al., 2022; Knopf et al., 2022, 2023). Figure 13 presents the $J_{het}(\Delta a_w)$ for the DIN and IMF data along with the parameterizations according to $log(J_{het}) = c \times \Delta a_w + d$. The values of c and d parameters are listed in Table 2. The Dust dominated sample has higher J_{het} at the same Δa_w compared with the other samples. The BBA influenced sample only nucleated ice at higher Δa_w. The DIN J_{het} for the FreshSS and AgedSS samples changes by 2 orders of magnitude within a wide range of Δa_w. For the FreshSS and AgedSS samples, IMF J_{het} with a larger c displays a steeper slope than DIN J_{het}.

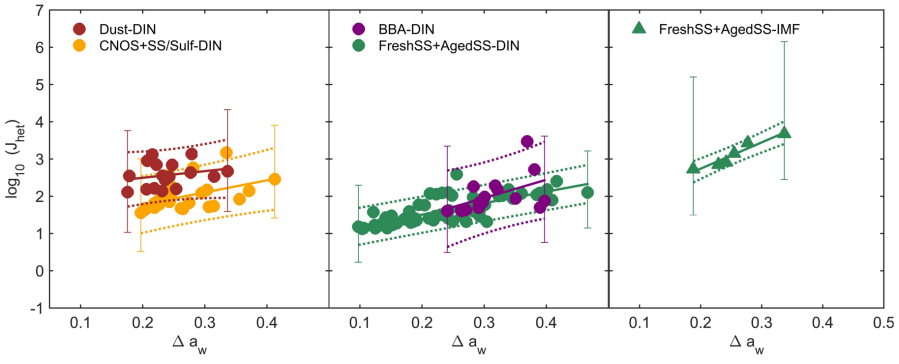

Figure 13. Heterogeneous ice nucleation rate coefficients (J_{het}) as a function of Δa_w. Brown, purple, orange, and green symbols represent Dust, BBA, CNOS and SS/Sulf, FreshSS and AgedSS dominated samples, respectively. Circles represent DIN and triangles represent IMF. Solid lines indicate the fittings according to $log(J_{het}) = c \times \Delta a_w + d$. Dashed lines represent the 95% prediction intervals. Only representative ΔJ_{het} (error bars) are plotted for better readability.

https://doi.org/10.5194/egusphere-2023-2646
Preprint. Discussion started: 13 November 2023

Table 2 The c and d values for the parameterizations of J_{het} as a function of Δa_w,

$$log(J_{het}) = c \times \Delta a_w + \mathrm{d}.$$

Sample type	c	LCL_c	UCL_c	d	LCL_d	UCL_d	RMSE
Dust-DIN	1.78	– 0.15	3.72	2.14	1.67	2.61	0.31
BBA-DIN	4.88	2.38	7.39	0.49	– 0.31	1.30	0.43
CNOS+SS/Sulf-DIN	3.24	1.91	4.57	1.13	0.77	1.50	0.35
FreshSS+AgedSS-DIN	3.09	2.76	3.42	0.89	0.81	0.97	0.24
FreshSS+AgedSS-IMF	7.06	6.03	8.09	1.33	1.06	1.60	0.09

A second method of parameterizing J_{het} is based on contact angles (θ) derived from CNT. We calculated θ for DIN following the our previous studies (Wang and Knopf, 2011; Wang et al., 2012a). θ is derived from J_{het}, the ice nucleation onset temperature and RH_{ice} using the following formula: $J_{het} = A \times e\left(\frac{-\Delta F_{g,het}}{kT}\right)$, where A is a pre-exponential factor and k is the Boltzmann constant. $\Delta F_{g,het}$ is the free energy of ice embryo formation defined as $\Delta F_{g,het} = \frac{16\pi M_w^2 \sigma_{i/v}^3}{3[RT\rho ln S_{ice}]^2} \times f(m)$, where R is the universal gas constant, ρ is the density of ice, S_{ice} is the ice saturation ratio ($S_{ice} = RH_{ice}/100\%$), M_w is the water molecular weight, $\sigma_{i/v}$ is the surface tension at the ice-vapor interface. $f(m)$ is the geometric factor and is defined as $f(m) = (m^3 - 3m + 2)/4$, where $m = cos\ (\theta)$. Smaller values of θ means higher ice nucleation efficiency and should translate to relatively lower values of RH_{ice} to observe ice nucleation in our experiments. Figure 14 represents mean θ as a function of temperature for INPs of all types of samples. When comparing θ at the same temperature, the FreshSS and AgedSS dominated samples in general have the smallest θ, followed by the Dust dominated, CNOS and SS/Sulf dominated, BBA influenced samples. For all the investigated samples, θ was relatively constant above 220 K and increased as temperature decreased to 205 K. In our previous study, θ was parameterized as a function of RH_{ice} including a set of various particle types (Wang and Knopf, 2011). θ for various particle types fall tightly into the parameterization. Here, we propose new parameterizations of θ as a function of $T^3 ln[RH_{ice}]^2$ to include the ice nucleation onset temperature and RH_{ice}, represented by $\theta = a + b \times ln(T^3 ln[RH_{ice}]^2 + c)$. As shown in Fig. 15, θ for the same particle types shows very similar trends. All fitting correlation coefficients, R^2, were larger than

https://doi.org/10.5194/egusphere-2023-2646
Preprint. Discussion started: 13 November 2023

0.99. The values of a, b, and c for each parameterization are listed in the Fig. 15. It is worth noting that the parameterization only applies to the DIN.

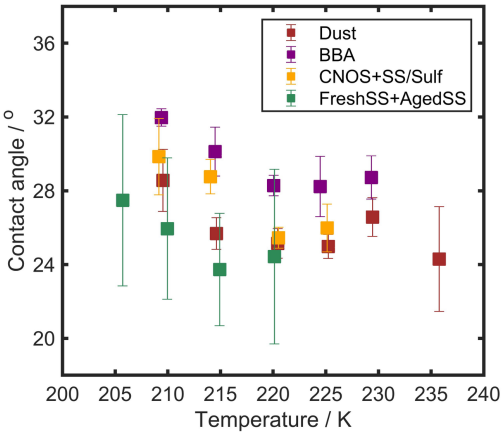

Figure 14. Mean values with one standard deviations of contact angle for DIN by the Dust, BBA, CNOS and SS/Sulf, FreshSS and AgedSS dominated samples.

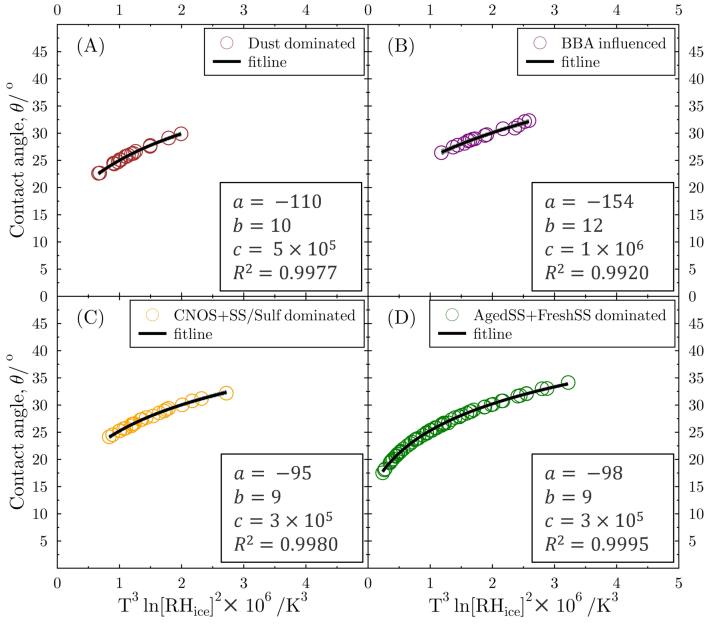

Figure 15. Parameterizations of θ as a function of $T^3 ln[RH_{ice}]^2$ including the ice nucleation onset temperature (T) and RH_{ice} for DIN by the Dust, BBA, CNOS and SS/Sulf, FreshSS and AgedSS dominated samples.

https://doi.org/10.5194/egusphere-2023-2646
Preprint. Discussion started: 13 November 2023

4 Atmospheric implications

We found that the distinct mixing states of particle populations were affected by several processes over different oceans. In the marine atmosphere that already has a contribution of sea salt particles, adding more fresh sea salt particles makes the population more internally mixed (Fig. 6). We suspect that much as it advects over open oceans where sea salt particle flux is large, the population will also be mostly internally mixed. Addition of new types of particles from other sources, such as dust storm (WP-I, S1, S2), biomass burning (WP-II, S14, S15), and secondary source (CNOS in SO region), will reduce the mixing state index and the population becomes more external mixing. These results are consistent with the proposed schematic description by Riemer et al. on the evolution of particle mixing state (Riemer et al., 2019). Aging of fresh sea salt particles leading to chlorine deficiencies were observed (Fig. 5). As discussed in Section 3.2, the selective or inhomogeneous aging processes on particles moves the population toward a more externally mixed state. Our study suggests that, when discussing the influence of the aging processes on the mixing state of ambient particles, it is necessary to consider whether the aging processes take place uniformly on all particles.

We characterized chemical compositions for particle population and INPs at single particle level. We found that all the identified particle types from different sources have the potential to serve as INPs, but have different ice nucleation efficiencies (Fig. 7 and Fig. 9). There is a growing notion in the ice nucleation community that all particles in an ambient particle population are capable of nucleating ice, and it is important to note that it is not in disagreement with measurements of frozen fractions or ice nucleating particles per volume of air. For example, consider all fresh sea spray particles had the potential to nucleate ice for 10 min of ice cloud formation at 220 K with $J_{het} = 10^1$ cm^{-2} s^{-1} in air having about 15 µm^2 cm^{-3} of surface area per volume of air. This corresponds to $\Delta a_w \sim 0.1$ in Fig. 13 and $RH_{ice} \sim 120\%$, resulting in an INP concentration ~ 1 L^{-1}. A larger Δa_w increases J_{het} and INP concentrations. Simply stated, all particles could

https://doi.org/10.5194/egusphere-2023-2646
Preprint. Discussion started: 13 November 2023

nucleate ice, but only a small fraction would. This INP concentration of 1 L^{-1} was shown to be sufficient to prevent homogeneous ice nucleation due to ice crystal growth causing water vapor depletion at updraft velocities below about 5 cm s^{-1}.

We found that S11 showed the highest ice nucleation efficiency among the FreshSS and AgedSS dominated samples (Fig. 7), which we attributed to the organic coatings on the particles. This indicates the importance of characterizing the physical mixing state of particles (i.e., morphology). INPs were enriched in only a single class, SS/Sulf class, which suggests that the aging process alters ice nucleation ability by changing the chemical mixing state of particles. Considering the characterizations of individual particles and INPs, the ice nucleation onset conditions, and the derived freezing kinetics, it is suggested that the ice nucleation abilities at cirrus conditions of these complex marine aerosols are affected not only by the particle compositions but also the mixing state of particle population. Future investigations are needed on how chemical and physical mixing state of particles impact ice nucleation in the atmosphere for a better understanding of aerosol-cloud interactions in the climate system.

According to SH and CNT, ice nucleation kinetic parameters, J_{het} and n_s, were derived from the experimental data. We derived parameterizations of n_s as a function of temperature for IMF and DIN of different dominated particle classes. We also proposed parameterizations of J_{het} as a function of Δa_w for IMF and DIN based on the water-activity based theory. In addition, θ was derived for DIN based on CNT. We propose new parameterizations of θ accounting both temperature and RH_{ice}. Despite the use of any parameterization, INP concentrations or ice crystal production rates can be estimated only if particle surface area data are available. These parameterizations of kinetic parameters can be used in cloud models using different ice nucleation descriptions to evaluate the potential sources and impacts of different particles on cloud formation in the marine atmosphere.

https://doi.org/10.5194/egusphere-2023-2646
Preprint. Discussion started: 13 November 2023

5 Conclusions

Composition, mixing state, and ice nucleation properties were investigated for the aerosol particles collected over the Western Pacific and Southern Ocean during a cruise in 2019 from South Korea (34.93°N) to Rose Sea (75.12°S). Seven particle classes were identified including the fresh sea salt, aged sea salt, sea salt mixed with sulfate, carbonaceous particle, sulfur-containing particle, dust, and mixture. Contributions of these particles varied over oceans at different latitudes. Except for the samples that were impacted by dust storm and biomass burning events, the fresh sea salt, aged sea salt, sea salt mixed with sulfate particles were the most prevalent particle types. Particles showed different degrees of chloride depletion resulting from the aging processes of acid displacements on fresh sea salt. Significant contributions of sulfur-containing particles were found in the Ross Sea, which was affected by phytoplankton blooms in austral summer. Mixing state index was positively correlated with the number percentages of fresh sea salt and negatively correlated with the proportion of sulfur-containing particles. Particle populations tended to be more internally mixed as the fresh sea salt fraction increases. When sea salt particles were a background or dominate particle type, inhomogeneous aging processes and new particle sources make the population more externally mixed.

We showed that different types of particle samples demonstrated a variety of ice nucleation abilities at cirrus conditions. The sample dominated by the fresh sea salt particles with organic coatings exhibited the highest ice nucleation efficiency with RH_{ice} onset as low as 121% whereas particles influenced by biomass burning were least efficient among the investigated samples. According to individual INP characterizations, the dominant particle types in the population all contribute to the identified INPs but with different enrichment factors. The sea salt mixed with sulfate particles were enriched in INPs with an overall factor of about 1.9. Ice nucleation abilities of marine aerosol particles were affected not only by composition but also the chemical and physical mixing state of particle population. Ice nucleation kinetic parameters, time

https://doi.org/10.5194/egusphere-2023-2646
Preprint. Discussion started: 13 November 2023

dependent J_{het}, time independent n_s, and contact angle, were derived from the experimental data and the corresponding parameterizations for different particle types are provided for cloud modeling. In this study, we demonstrated the diversity in the particle characteristics at single particle level, mixing state of particle population, and particles' abilities to form ice crystals in different marine atmosphere in both northern and southern hemispheres. The results motivate the need of further investigations on how mixing state of particles impact ice nucleation in the atmosphere.

Data availability. All data are given in the main text or in the Supplement. HYSPLIT data were obtained through the NOAA website (https://www.ready.noaa.gov/hypub-bin/trajasrc.pl). NAAPS aerosol reanalysis data were obtained from https://nrlgodae1.nrlmry.navy.mil/ftp/outgoing/nrl/NAAPS-REANALYSIS/. FIRMS data were obtained from https://firms.modaps.eosdis.nasa.gov/.

Supplement. The supplement related to this article is available online.

Author contributions. XJ performed the experiments and wrote the first draft of the manuscript. XJ, TZ, JP, and BW performed the data analysis. JP and KP collected the samples. BW, JP and KP initiated and designed the study. BW supervised the project. BW, YJY, and XJ led the discussion and all authors contributed to the data interpretation and the manuscript writing.

Competing interests. The authors declare that they have no conflict of interest.

Acknowledgements. BW, XJ, and TZ thank the support by National Science Foundation of China (42075076, 41775133), Fundamental Research Funds for the Central Universities (20720160111, 20720190147). This study is also partially funded by the Korea Polar Research Institute research grant (PE23110, PE23030). BW and JY thank the support by the Fund of Key Laboratory of Global Change and

https://doi.org/10.5194/egusphere-2023-2646
Preprint. Discussion started: 13 November 2023

Marine-Atmospheric Chemistry, MNR (GCMAC2004). TZ acknowledges the support by the PhD Fellowship of the State Key Laboratory of Marine Environmental Science at Xiamen University. We thank the staff onboard R/V *Araon* helping the sampling during the Antarctic cruise and Peter A. Alpert for helpful discussion and manuscript revision.

References

Adachi, K., Oshima, N., Gong, Z., de Sá, S., Bateman, A. P., Martin, S. T., de Brito, J. F., Artaxo, P., Cirino, G. G., Sedlacek III, A. J., and Buseck, P. R.: Mixing states of Amazon basin aerosol particles transported over long distances using transmission electron microscopy, Atmos. Chem. Phys., 20, 11923–11939, https://doi.org/10.5194/acp-20-11923-2020, 2020.

Alpert, P. A. and Knopf, D. A.: Analysis of isothermal and cooling-rate-dependent immersion freezing by a unifying stochastic ice nucleation model, Atmos. Chem. Phys., 16, 2083–2107, https://doi.org/10.5194/acp-16-2083-2016, 2016.

Alpert, P. A., Kilthau, W. P., O'Brien, R. E., Moffet, R. C., Gilles, M. K., Wang, B., Laskin, A., Aller, J. Y., and Knopf, D. A.: Ice-nucleating agents in sea spray aerosol identified and quantified with a holistic multimodal freezing model, Sci. Adv., 8, eabq6842, https://doi.org/10.1126/sciadv.abq6842, 2022.

Angle, K. J., Crocker, D. R., Simpson, R. M. C., Mayer, K. J., Garofalo, L. A., Moore, A. N., Mora Garcia, S. L., Or, V. W., Srinivasan, S., Farhan, M., Sauer, J. S., Lee, C., Pothier, M. A., Farmer, D. K., Martz, T. R., Bertram, T. H., Cappa, C. D., Prather, K. A., and Grassian, V. H.: Acidity across the interface from the ocean surface to sea spray aerosol, Proc. Natl. Acad. Sci., 118, e2018397118, https://doi.org/10.1073/pnas.2018397118, 2021.

Ault, A. P., Moore, M. J., Furutani, H., and Prather, K. A.: Impact of emissions from the Los Angeles Port Region on San Diego air quality during regional transport events, Environ. Sci. Technol., 43, 3500–3506, https://doi.org/10/d7kt9s, 2009.

Ault, A. P., Gaston, C. J., Wang, Y., Dominguez, G., Thiemens, M. H., and Prather, K. A.: Characterization of the single particle mixing state of individual ship plume events measured at the port of los angeles, Environ. Sci. Technol., 44, 1954–1961, https://doi.org/10.1021/es902985h, 2010.

Barnes, I., Hjorth, J., and Mihalopoulos, N.: Dimethyl sulfide and dimethyl sulfoxide and their oxidation in the atmosphere, Chem. Rev., 106, 940–975, https://doi.org/10.1021/cr020529+, 2006.

Beck, L. J., Sarnela, N., Junninen, H., Hoppe, C. J. M., Garmash, O., Bianchi, F., Riva, M., Rose,

https://doi.org/10.5194/egusphere-2023-2646
Preprint. Discussion started: 13 November 2023

C., Peräkylä, O., Wimmer, D., Kausiala, O., Jokinen, T., Ahonen, L., Mikkilä, J., Hakala, J., He, X., Kontkanen, J., Wolf, K. K. E., Cappelletti, D., Mazzola, M., Traversi, R., Petroselli, C., Viola, A. P., Vitale, V., Lange, R., Massling, A., Nøjgaard, J. K., Krejci, R., Karlsson, L., Zieger, P., Jang, S., Lee, K., Vakkari, V., Lampilahti, J., Thakur, R. C., Leino, K., Kangasluoma, J., Duplissy, E., Siivola, E., Marbouti, M., Tham, Y. J., Saiz-Lopez, A., Petäjä, T., Ehn, M., Worsnop, D. R., Skov, H., Kulmala, M., Kerminen, V., and Sipilä, M.: Differing mechanisms of new particle formation at two arctic sites, Geophys. Res. Lett., 48, https://doi.org/10.1029/2020GL091334, 2021.

Berndt, T., Hoffmann, E. H., Tilgner, A., Stratmann, F., and Herrmann, H.: Direct sulfuric acid formation from the gas-phase oxidation of reduced-sulfur compounds, Nat. Commun., 14, 4849, https://doi.org/10/gs3whz, 2023.

Boreddy, S. K. R. and Kawamura, K.: A 12-year observation of water-soluble ions in TSP aerosols collected at a remote marine location in the western North Pacific: an outflow region of Asian dust, Atmos. Chem. Phys., 15, 6437–6453, https://doi.org/10.5194/acp-15-6437-2015, 2015.

Burrows, S. M., McCluskey, C. S., Cornwell, G., Steinke, I., Zhang, K., Zhao, B., Zawadowicz, M., Raman, A., Kulkarni, G., China, S., Zelenyuk, A., and DeMott, P. J.: Ice-nucleating particles that impact clouds and climate: observational and modeling research needs, Rev. Geophys., 60, https://doi.org/10.1029/2021RG000745, 2022.

Charnawskas, J. C., Alpert, P. A., Lambe, A. T., Berkemeier, T., O' Brien, R. E., Massoli, P., Onasch, T. B., Shiraiwa, M., Moffet, R. C., Gilles, M. K., Davidovits, P., Worsnop, D. R., and Knopf, D. A.: Condensed-phase biogenic-anthropogenic interactions with implications for cold cloud formation, Faraday Discuss., 200, 165–194, https://doi.org/10.1039/C7FD00010C, 2017.

Chen, J., Li, C., Ristovski, Z., Milic, A., Gu, Y., Islam, M. S., Wang, S., Hao, J., Zhang, H., He, C., Guo, H., Fu, H., Miljevic, B., Morawska, L., Thai, P., Lam, Y. F., Pereira, G., Ding, A., Huang, X., and Dumka, U. C.: A review of biomass burning: Emissions and impacts on air quality, health and climate in China, Sci. Total Environ., 579, 1000–1034, https://doi.org/10.1016/j.scitotenv.2016.11.025, 2017.

Chen, Q., Sherwen, T., Evans, M., and Alexander, B.: DMS oxidation and sulfur aerosol formation in the marine troposphere: a focus on reactive halogen and multiphase chemistry, Atmos. Chem. Phys., 18, 13617–13637, https://doi.org/10.5194/acp-18-13617-2018, 2018.

China, S., Alpert, P. A., Zhang, B., Schum, S., Dzepina, K., Wright, K., Owen, R. C., Fialho, P., Mazzoleni, L. R., Mazzoleni, C., and Knopf, D. A.: Ice cloud formation potential by free tropospheric particles from long-range transport over the Northern Atlantic Ocean, J. Geophys. Res. Atmos., 122, 3065–3079, https://doi.org/10.1002/2016JD025817, 2017.

China, S., Burrows, S. M., Wang, B., Harder, T. H., Weis, J., Tanarhte, M., Rizzo, L. V., Brito, J., Cirino, G. G., Ma, P.-L., Cliff, J., Artaxo, P., Gilles, M. K., and Laskin, A.: Fungal spores as a source of sodium salt particles in the Amazon basin, Nat. Commun., 9, 4793, https://doi.org/10.1038/s41467-018-07066-4, 2018.

https://doi.org/10.5194/egusphere-2023-2646
Preprint. Discussion started: 13 November 2023

1087 Chou, C., Kanji, Z. A., Stetzer, O., Tritscher, T., Chirico, R., Heringa, M. F., Weingartner, E., Prévôt,
1088 A. S. H., Baltensperger, U., and Lohmann, U.: Effect of photochemical ageing on the ice
1089 nucleation properties of diesel and wood burning particles, Atmos. Chem. Phys., 13, 761–772,
1090 https://doi.org/10.5194/acp-13-761-2013, 2013.

1091 Cochran, R. E., Ryder, O. S., Grassian, V. H., and Prather, K. A.: Sea spray aerosol: the chemical
1092 link between the oceans, atmosphere, and climate, Acc. Chem. Res., 50, 599–604,
1093 https://doi.org/10.1021/acs.accounts.6b00603, 2017.

1094 Connolly, P. J., Möhler, O., Field, P. R., Saathoff, H., Burgess, R., Choularton, T., and Gallagher,
1095 M.: Studies of heterogeneous freezing by three different desert dust samples, Atmos. Chem.
1096 Phys., https://doi.org/10.5194/acp-9-2805-2009, 2009.

1097 Cziczo, D. J., Ladino, L., Boose, Y., Kanji, Z. A., Kupiszewski, P., Lance, S., Mertes, S., and Wex,
1098 H.: Measurements of ice nucleating particles and ice residuals, Meteorol. Monogr., 58, 8.1-
1099 8.13, https://doi.org/10.1175/AMSMONOGRAPHS-D-16-0008.1, 2017.

1100 DeMott, P. J., Chen, Y., Kreidenweis, S. M., Rogers, D. C., and Sherman, D. E.: Ice formation by
1101 black carbon particles, Geophys. Res. Lett., 26, 2429–2432,
1102 https://doi.org/10.1029/1999GL900580, 1999.

1103 DeMott, P. J., Petters, M. D., Prenni, A. J., Carrico, C. M., Kreidenweis, S. M., Collett, J. L., and
1104 Moosmüller, H.: Ice nucleation behavior of biomass combustion particles at cirrus
1105 temperatures, J. Geophys. Res., 114, 2009JD012036, https://doi.org/10.1029/2009JD012036,
1106 2009.

1107 Ditas, J., Ma, N., Zhang, Y., Assmann, D., Neumaier, M., Riede, H., Karu, E., Williams, J., Scharffe,
1108 D., Wang, Q., Saturno, J., Schwarz, J. P., Katich, J. M., McMeeking, G. R., Zahn, A., Hermann,
1109 M., Brenninkmeijer, C. A. M., Andreae, M. O., Pöschl, U., Su, H., and Cheng, Y.: Strong impact
1110 of wildfires on the abundance and aging of black carbon in the lowermost stratosphere, Proc.
1111 Natl. Acad. Sci., 115, https://doi.org/10.1073/pnas.1806868115, 2018.

1112 Ervens, B., Sorooshian, A., Aldhaif, A. M., Shingler, T., Crosbie, E., Ziemba, L., Campuzano-Jost,
1113 P., Jimenez, J. L., and Wisthaler, A.: Is there an aerosol signature of chemical cloud processing?,
1114 Atmos. Chem. Phys., 18, 16099–16119, https://doi.org/10.5194/acp-18-16099-2018, 2018.

1115 Fraund, M., Pham, D., Bonanno, D., Harder, T., Wang, B., Brito, J., de Sá, S., Carbone, S., China,
1116 S., Artaxo, P., Martin, S., Pöhlker, C., Andreae, M., Laskin, A., Gilles, M., and Moffet, R.: Elemental
1117 mixing state of aerosol particles collected in central Amazonia during GoAmazon2014/15,
1118 Atmosphere, 8, 173, https://doi.org/10.3390/atmos8090173, 2017.

1119 Fu, P. Q., Kawamura, K., Chen, J., Charrière, B., and Sempéré, R.: Organic molecular
1120 composition of marine aerosols over the Arctic Ocean in summer: contributions of primary
1121 emission and secondary aerosol formation, Biogeosciences, 10, 653–667,
1122 https://doi.org/10.5194/bg-10-653-2013, 2013.

1123 Fuzzi, S., Decesari, S., Facchini, M. C., Cavalli, F., Emblico, L., Mircea, M., Andreae, M. O., Trebs,

https://doi.org/10.5194/egusphere-2023-2646
Preprint. Discussion started: 13 November 2023

I., Hoffer, A., Guyon, P., Artaxo, P., Rizzo, L. V., Lara, L. L., Pauliquevis, T., Maenhaut, W., Raes, N., Chi, X., Mayol-Bracero, O. L., Soto-García, L. L., Claeys, M., Kourtchev, I., Rissler, J., Swietlicki, E., Tagliavini, E., Schkolnik, G., Falkovich, A. H., Rudich, Y., Fisch, G., and Gatti, L. V.: Overview of the inorganic and organic composition of size-segregated aerosol in Rondônia, Brazil, from the biomass-burning period to the onset of the wet season, J. Geophys. Res., 112, 2005JD006741, https://doi.org/10.1029/2005JD006741, 2007.

Geng, X., Zhong, G., Li, J., Cheng, Z., Mo, Y., Mao, S., Su, T., Jiang, H., Ni, K., and Zhang, G.: Molecular marker study of aerosols in the northern South China Sea: Impact of atmospheric outflow from the Indo-China Peninsula and South China, Atmos. Environ., 206, 225–236, https://doi.org/10.1016/j.atmosenv.2019.02.033, 2019.

Han, Y., Fang, X., Xi, X., Song, L., and Yang, S.: Dust storm in Asia continent and its bio-environmental effects in the North Pacific: A case study of the strongest dust event in April, 2001 in central Asia, Sci. Bull., 51, 723–730, https://doi.org/10.1007/s11434-006-0723-2, 2006.

Healy, R. M., Sciare, J., Poulain, L., Crippa, M., Wiedensohler, A., Prévôt, A. S. H., Baltensperger, U., Sarda-Estève, R., McGuire, M. L., Jeong, C.-H., McGillicuddy, E., O' Connor, I. P., Sodeau, J. R., Evans, G. J., and Wenger, J. C.: Quantitative determination of carbonaceous particle mixing state in Paris using single-particle mass spectrometer and aerosol mass spectrometer measurements, Atmos. Chem. Phys., 13, 9479–9496, https://doi.org/10.5194/acp-13-9479-2013, 2013.

Hirsch, E. and Koren, I.: Record-breaking aerosol levels explained by smoke injection into the stratosphere, Science, 371, 1269–1274, https://doi.org/10.1126/science.abe1415, 2021.

Hodshire, A. L., Akherati, A., Alvarado, M. J., Brown-Steiner, B., Jathar, S. H., Jimenez, J. L., Kreidenweis, S. M., Lonsdale, C. R., Onasch, T. B., Ortega, A. M., and Pierce, J. R.: Aging effects on biomass burning aerosol mass and composition: a critical review of field and laboratory studies, Environ. Sci. Technol., 53, 10007–10022, https://doi.org/10.1021/acs.est.9b02588, 2019.

Hoose, C. and Möhler, O.: Heterogeneous ice nucleation on atmospheric aerosols: a review of results from laboratory experiments, Atmos. Chem. Phys., 12, 9817–9854, https://doi.org/10.5194/acp-12-9817-2012, 2012.

Hopkins, R. J., Desyaterik, Y., Tivanski, A. V., Zaveri, R. A., Berkowitz, C. M., Tyliszczak, T., Gilles, M. K., and Laskin, A.: Chemical speciation of sulfur in marine cloud droplets and particles: Analysis of individual particles from the marine boundary layer over the California current, J. Geophys. Res., 113, D04209, https://doi.org/10.1029/2007JD008954, 2008.

Inoue, J., Tobo, Y., Taketani, F., and Sato, K.: Oceanic supply of ice-nucleating particles and its effect on ice cloud formation: a case study in the arctic ocean during a cold-air outbreak in early winter, Geophys. Res. Lett., 48, https://doi.org/10.1029/2021GL094646, 2021.

https://doi.org/10.5194/egusphere-2023-2646
Preprint. Discussion started: 13 November 2023

1161 Jang, J., Park, J., Park, J., Yoon, Y. J., Dall'Osto, M., Park, K.-T., Jang, E., Lee, J. Y., Cho, K. H., and
1162 Lee, B. Y.: Ocean-atmosphere interactions: Different organic components across Pacific and
1163 Southern Oceans, Sci. Total Environ., 878, 162969, https://doi.org/10/gs3zkw, 2023.

1164 Kanji, Z. A., DeMott, P. J., Möhler, O., and Abbatt, J. P. D.: Results from the University of Toronto
1165 continuous flow diffusion chamber at ICIS 2007: instrument intercomparison and ice onsets
1166 for different aerosol types, Atmos. Chem. Phys., 11, 31–41, https://doi.org/10.5194/acp-11-
1167 31-2011, 2011.

1168 Kanji, Z. A., Ladino, L. A., Wex, H., Boose, Y., Burkert-Kohn, M., Cziczo, D. J., and Krämer, M.:
1169 Overview of ice nucleating particles, Meteorol. Monogr., 58, 1.1-1.33,
1170 https://doi.org/10.1175/AMSMONOGRAPHS-D-16-0006.1, 2017.

1171 Knopf, D. A. and Alpert, P. A.: A water activity based model of heterogeneous ice nucleation
1172 kinetics for freezing of water and aqueous solution droplets, Faraday Discuss., 165, 513,
1173 https://doi.org/10.1039/c3fd00035d, 2013.

1174 Knopf, D. A., Alpert, P. A., Wang, B., and Aller, J. Y.: Stimulation of ice nucleation by marine
1175 diatoms, Nat. Geosci., 4, 88–90, https://doi.org/10.1038/ngeo1037, 2011.

1176 Knopf, D. A., Alpert, P. A., Wang, B., O' Brien, R. E., Kelly, S. T., Laskin, A., Gilles, M. K., and
1177 Moffet, R. C.: Microspectroscopic imaging and characterization of individually identified ice
1178 nucleating particles from a case field study, J. Geophys. Res. Atmos., 119, 10,365-10,381,
1179 https://doi.org/10.1002/2014JD021866, 2014.

1180 Knopf, D. A., Alpert, P. A., and Wang, B.: The role of organic aerosol in atmospheric ice
1181 nucleation: a review, ACS Earth Space Chem., 2, 168–202,
1182 https://doi.org/10.1021/acsearthspacechem.7b00120, 2018.

1183 Knopf, D. A., Charnawskas, J. C., Wang, P., Wong, B., Tomlin, J. M., Jankowski, K. A., Fraund,
1184 M., Veghte, D. P., China, S., Laskin, A., Moffet, R. C., Gilles, M. K., Aller, J. Y., Marcus, M. A.,
1185 Raveh-Rubin, S., and Wang, J.: Micro-spectroscopic and freezing characterization of ice-
1186 nucleating particles collected in the marine boundary layer in the eastern North Atlantic,
1187 Atmos. Chem. Phys., 22, 5377–5398, https://doi.org/10.5194/acp-22-5377-2022, 2022.

1188 Knopf, D. A., Wang, P., Wong, B., Tomlin, J. M., Veghte, D. P., Lata, N. N., China, S., Laskin, A.,
1189 Moffet, R. C., Aller, J. Y., Marcus, M. A., and Wang, J.: Physicochemical characterization of free
1190 troposphere and marine boundary layer ice-nucleating particles collected by aircraft in the
1191 eastern North Atlantic, Atmos. Chem. Phys., 23, 8659–8681, https://doi.org/10.5194/acp-23-
1192 8659-2023, 2023.

1193 Koehler, K. A., DeMott, P. J., Kreidenweis, S. M., Popovicheva, O. B., Petters, M. D., Carrico, C.
1194 M., Kireeva, E. D., Khokhlova, T. D., and Shonija, N. K.: Cloud condensation nuclei and ice
1195 nucleation activity of hydrophobic and hydrophilic soot particles, Phys. Chem. Chem. Phys.,
1196 11, 7906, https://doi.org/10.1039/b905334b, 2009.

1197 Koop, T. and Zobrist, B.: Parameterizations for ice nucleation in biological and atmospheric

https://doi.org/10.5194/egusphere-2023-2646
Preprint. Discussion started: 13 November 2023

systems, Phys. Chem. Chem. Phys., 11, 10839, https://doi.org/10.1039/b914289d, 2009.

Koop, T., Luo, B., Tsias, A., and Peter, T.: Water activity as the determinant for homogeneous ice nucleation in aqueous solutions, Nature, 406, 611–614, https://doi.org/10.1038/35020537, 2000.

Kulkarni, G., Sanders, C., Zhang, K., Liu, X., and Zhao, C.: Ice nucleation of bare and sulfuric acid-coated mineral dust particles and implication for cloud properties: Ice formation on dust particles, J. Geophys. Res. Atmos., 119, 9993–10011, https://doi.org/10.1002/2014JD021567, 2014.

Kunwar, B., Pokhrel, A., Niwai, T., and Kawamura, K.: Spatial and longitudinal distributions of total carbon, nitrogen and sulfur together with water-soluble major ions in marine aerosols collected from the western pacific and southern ocean, J. Geophys. Res., 128, e2022JD037874, https://doi.org/10.1029/2022JD037874, 2023.

Laskin, A., Iedema, M. J., and Cowin, J. P.: Quantitative time-resolved monitoring of nitrate formation in sea salt particles using a CCSEM/EDX single particle analysis, Environ. Sci. Technol., 36, 4948–4955, https://doi.org/10.1021/es020551k, 2002.

Laskin, A., Cowin, J. P., and Iedema, M. J.: Analysis of individual environmental particles using modern methods of electron microscopy and X-ray microanalysis, J. Electron. Spectrosc. Relat. Phenom., 150, 260–274, https://doi.org/10.1016/j.elspec.2005.06.008, 2006.

Laskin, A., Moffet, R. C., Gilles, M. K., Fast, J. D., Zaveri, R. A., Wang, B., Nigge, P., and Shutthanandan, J.: Tropospheric chemistry of internally mixed sea salt and organic particles: Surprising reactivity of NaCl with weak organic acids, J. Geophys. Res., 117, https://doi.org/10.1029/2012JD017743, 2012.

Lata, N. N., Zhang, B., Schum, S., Mazzoleni, L., Brimberry, R., Marcus, M. A., Cantrell, W. H., Fialho, P., Mazzoleni, C., and China, S.: Aerosol composition, mixing state, and phase state of free tropospheric particles and their role in ice cloud formation, ACS Earth Space Chem., 5, 3499–3510, https://doi.org/10.1021/acsearthspacechem.1c00315, 2021.

de Leeuw, G., Andreas, E. L., Anguelova, M. D., Fairall, C. W., Lewis, E. R., O' Dowd, C., Schulz, M., and Schwartz, S. E.: Production flux of sea spray aerosol, Rev. Geophys., 49, RG2001, https://doi.org/10.1029/2010RG000349, 2011.

Liu, Y., Minofar, B., Desyaterik, Y., Dames, E., Zhu, Z., Cain, J. P., Hopkins, R. J., Gilles, M. K., Wang, H., Jungwirth, P., and Laskin, A.: Internal structure, hygroscopic and reactive properties of mixed sodium methanesulfonate-sodium chloride particles, Phys. Chem. Chem. Phys., 13, 11846, https://doi.org/10.1039/c1cp20444k, 2011.

MacKay, D. J. C.: Information theory, inference, and learning algorithms, Cambridge University Press, Cambridge, UK ; New York, 628 pp., 2003.

Masson-Delmotte, V., Zhai, P., Pirani, A., Connors, S. L., Péan, C., Berger, S., Caud, Chen, Y.,

https://doi.org/10.5194/egusphere-2023-2646
Preprint. Discussion started: 13 November 2023

Goldfarb, L., Gomis, M. I., Huang, M., Leitzell, K., Lonnoy, E., Matthews, J. B. R., Maycock, T. K., Waterfield, T., Yelekçi, O., Yu, R., and Zhou, B.: Climate change 2021: the physical science basis. Contribution of working group I to the sixth assessment report of the intergovernmental panel on climate change, Cambridge University Press, 2021.

McCluskey, C. S., Hill, T. C. J., Humphries, R. S., Rauker, A. M., Moreau, S., Strutton, P. G., Chambers, S. D., Williams, A. G., McRobert, I., Ward, J., Keywood, M. D., Harnwell, J., Ponsonby, W., Loh, Z. M., Krummel, P. B., Protat, A., Kreidenweis, S. M., and DeMott, P. J.: Observations of ice nucleating particles over Southern Ocean waters, Geophys. Res. Lett., 45, https://doi.org/10.1029/2018GL079981, 2018.

Möhler, O., Büttner, S., Linke, C., Schnaiter, M., Saathoff, H., Stetzer, O., Wagner, R., Krämer, M., Mangold, A., Ebert, V., and Schurath, U.: Effect of sulfuric acid coating on heterogeneous ice nucleation by soot aerosol particles, J. Geophys. Res., 110, https://doi.org/10.1029/2004JD005169, 2005a.

Möhler, O., Linke, C., Saathoff, H., Schnaiter, M., Wagner, R., Mangold, A., Krämer, M., and Schurath, U.: Ice nucleation on flame soot aerosol of different organic carbon content, Meteorol. Zeitschrift, 14, 477–484, https://doi.org/10.1127/0941-2948/2005/0055, 2005b.

Murray, B. J., O'Sullivan, D., Atkinson, J. D., and Webb, M. E.: Ice nucleation by particles immersed in supercooled cloud droplets, Chem. Soc. Rev., 41, 6519, https://doi.org/10.1039/c2cs35200a, 2012.

Myriokefalitakis, S., Vignati, E., Tsigaridis, K., Papadimas, C., Sciare, J., Mihalopoulos, N., Facchini, M. C., Rinaldi, M., Dentener, F. J., Ceburnis, D., Hatzianastasiou, N., O' Dowd, C. D., van Weele, M., and Kanakidou, M.: Global modeling of the oceanic source of organic aerosols, Adv. Meteorol., 2010, 1–16, https://doi.org/10.1155/2010/939171, 2010.

O'Brien, R. E., Wang, B., Laskin, A., Riemer, N., West, M., Zhang, Q., Sun, Y., Yu, X., Alpert, P., Knopf, D. A., Gilles, M. K., and Moffet, R. C.: Chemical imaging of ambient aerosol particles: Observational constraints on mixing state parameterization, J. Geophys. Res. Atmos., 120, 9591–9605, https://doi.org/10.1002/2015JD023480, 2015.

Palm, B. B., Peng, Q., Fredrickson, C. D., Lee, B. H., Garofalo, L. A., Pothier, M. A., Kreidenweis, S. M., Farmer, D. K., Pokhrel, R. P., Shen, Y., Murphy, S. M., Permar, W., Hu, L., Campos, T. L., Hall, S. R., Ullmann, K., Zhang, X., Flocke, F., Fischer, E. V., and Thornton, J. A.: Quantification of organic aerosol and brown carbon evolution in fresh wildfire plumes, Proc. Natl. Acad. Sci. U.S.A., 117, 29469–29477, https://doi.org/10.1073/pnas.2012218117, 2020.

Park, J., Dall'Osto, M., Park, K., Gim, Y., Kang, H. J., Jang, E., Park, K.-T., Park, M., Yum, S. S., Jung, J., Lee, B. Y., and Yoon, Y. J.: Shipborne observations reveal contrasting Arctic marine, Arctic terrestrial and Pacific marine aerosol properties, Atmos. Chem. Phys., 20, 5573–5590, https://doi.org/10.5194/acp-20-5573-2020, 2020.

Park, J. Y., Lim, S., and Park, K.: Mixing state of submicrometer sea spray particles enriched by

https://doi.org/10.5194/egusphere-2023-2646
Preprint. Discussion started: 13 November 2023

1271 insoluble species in bubble-bursting experiments, J. Atmos. Ocean. Technol., 31, 93–104,
1272 https://doi.org/10.1175/JTECH-D-13-00086.1, 2014.

1273 Primm, K. M., Schill, G. P., Veghte, D. P., Freedman, M. A., and Tolbert, M. A.: Depositional ice
1274 nucleation on NX illite and mixtures of NX illite with organic acids, J. Atmos. Chem., 74, 55–
1275 69, https://doi.org/10.1007/s10874-016-9340-x, 2017.

1276 Pruppacher, H. R. and Klett, J. D.: Microphysics of clouds and precipitation, Springer
1277 Netherlands, Dordrecht, https://doi.org/10.1007/978-0-306-48100-0, 2010.

1278 Riemer, N. and West, M.: Quantifying aerosol mixing state with entropy and diversity
1279 measures, Atmos. Chem. Phys., 13, 11423–11439, https://doi.org/10.5194/acp-13-11423-
1280 2013, 2013.

1281 Riemer, N., Ault, A. P., West, M., Craig, R. L., and Curtis, J. H.: Aerosol mixing state:
1282 measurements, modeling, and impacts, Rev. Geophys., 57, 187–249,
1283 https://doi.org/10.1029/2018RG000615, 2019.

1284 Rolph, G., Stein, A., and Stunder, B.: Real-time environmental applications and display system:
1285 ready, Environ. Model Softw., 95, 210–228, https://doi.org/10.1016/j.envsoft.2017.06.025,
1286 2017.

1287 Sasakawa, M. and Uematsu, M.: Chemical composition of aerosol, sea fog, and rainwater in
1288 the marine boundary layer of the northwestern North Pacific and its marginal seas, J. Geophys.
1289 Res., 107, https://doi.org/10.1029/2001JD001004, 2002.

1290 Schill, G. P. and Tolbert, M. A.: Heterogeneous ice nucleation on simulated sea-spray aerosol
1291 using raman microscopy, J. Phys. Chem. C, 118, 29234–29241,
1292 https://doi.org/10.1021/jp505379j, 2014.

1293 Song, Y., Qiao, F., Liu, J., Shu, Q., Bao, Y., Wei, M., and Song, Z.: Effects of sea spray on large-
1294 scale climatic features over the southern ocean, J. Clim., 35, 4645–4663,
1295 https://doi.org/10.1175/JCLI-D-21-0608.1, 2022.

1296 Stein, A. F., Draxler, R. R., Rolph, G. D., Stunder, B. J. B., Cohen, M. D., and Ngan, F.: Noaa' s
1297 HYSPLIT atmospheric transport and dispersion modeling system, Bull. Am. Meteorol. Soc., 96,
1298 2059–2077, https://doi.org/10.1175/BAMS-D-14-00110.1, 2015.

1299 Stocker, T. F., Qin, D., Plattner, G.-K., Tignor, M. M. B., Allen, S. K., Boschung, J., Nauels, A., Xia,
1300 Y., Bex, V., and Midgley, P. M.: Climate change 2013: the physical science basis. Contribution
1301 of working group I to the fifth assessment report of the intergovernmental panel on climate
1302 change, Cambridge University Press, 2013.

1303 Su, B., Wang, T., Zhang, G., Liang, Y., Lv, C., Hu, Y., Li, L., Zhou, Z., Wang, X., and Bi, X.: A review
1304 of atmospheric aging of sea spray aerosols: potential factors affecting chloride depletion,
1305 Atmos. Environ., 290, 119365, https://doi.org/10.1016/j.atmosenv.2022.119365, 2022.

https://doi.org/10.5194/egusphere-2023-2646
Preprint. Discussion started: 13 November 2023

1306 Tang, M., Cziczo, D. J., and Grassian, V. H.: Interactions of water with mineral dust aerosol:
1307 water adsorption, hygroscopicity, cloud condensation, and ice nucleation, Chem. Rev., 116,
1308 4205–4259, https://doi.org/10.1021/acs.chemrev.5b00529, 2016.

1309 Tomlin, J. M., Jankowski, K. A., Veghte, D. P., China, S., Wang, P., Fraund, M., Weis, J., Zheng,
1310 G., Wang, Y., Rivera-Adorno, F., Raveh-Rubin, S., Knopf, D. A., Wang, J., Gilles, M. K., Moffet,
1311 R. C., and Laskin, A.: Impact of dry intrusion events on the composition and mixing state of
1312 particles during the winter Aerosol and Cloud Experiment in the Eastern North Atlantic (ACE-
1313 ENA), Atmos. Chem. Phys., 21, 18123–18146, https://doi.org/10.5194/acp-21-18123-2021,
1314 2021.

1315 Tomlin, J. M., Weis, J., Veghte, D. P., China, S., Fraund, M., He, Q., Reicher, N., Li, C., Jankowski,
1316 K. A., Rivera-Adorno, F. A., Morales, A. C., Rudich, Y., Moffet, R. C., Gilles, M. K., and Laskin, A.:
1317 Chemical composition and morphological analysis of atmospheric particles from an intensive
1318 bonfire burning festival, Environ. Sci.: Atmos., 2, 616–633,
1319 https://doi.org/10.1039/D2EA00037G, 2022.

1320 Vali, G.: Qauantitative evaluation of experimental results on the heterogeneous freezing
1321 nucleation of supercooled liquids, J. Atmos. Sci., 28, 402–409, https://doi.org/10.1175/1520-
1322 0469(1971)028<0402:QEOERA>2.0.CO;2, 1971.

1323 Wagner, R., Kaufmann, J., Möhler, O., Saathoff, H., Schnaiter, M., Ullrich, R., and Leisner, T.:
1324 Heterogeneous ice nucleation ability of NaCl and sea salt aerosol particles at cirrus
1325 temperatures, J. Geophys. Res. Atmos., 123, 2841–2860,
1326 https://doi.org/10.1002/2017JD027864, 2018.

1327 Wang, B. and Knopf, D. A.: Heterogeneous ice nucleation on particles composed of humic-
1328 like substances impacted by O_3, J. Geophys. Res., 116, D03205,
1329 https://doi.org/10.1029/2010JD014964, 2011.

1330 Wang, B., Laskin, A., Roedel, T., Gilles, M. K., Moffet, R. C., Tivanski, A. V., and Knopf, D. A.:
1331 Heterogeneous ice nucleation and water uptake by field-collected atmospheric particles
1332 below 273 K, J. Geophys. Res., 117, n/a-n/a, https://doi.org/10.1029/2012JD017446, 2012a.

1333 Wang, B., Lambe, A. T., Massoli, P., Onasch, T. B., Davidovits, P., Worsnop, D. R., and Knopf, D.
1334 A.: The deposition ice nucleation and immersion freezing potential of amorphous secondary
1335 organic aerosol: Pathways for ice and mixed-phase cloud formation, J. Geophys. Res., 117,
1336 n/a-n/a, https://doi.org/10.1029/2012JD018063, 2012b.

1337 Wang, B., O'Brien, R. E., Kelly, S. T., Shilling, J. E., Moffet, R. C., Gilles, M. K., and Laskin, A.:
1338 Reactivity of liquid and semisolid secondary organic carbon with chloride and nitrate in
1339 atmospheric aerosols, J. Phys. Chem. A, 119, 4498–4508, https://doi.org/10.1021/jp510336q,
1340 2015.

1341 Wang, B., Harder, T. H., Kelly, S. T., Piens, D. S., China, S., Kovarik, L., Keiluweit, M., Arey, B. W.,
1342 Gilles, M. K., and Laskin, A.: Airborne soil organic particles generated by precipitation, Nat.

https://doi.org/10.5194/egusphere-2023-2646
Preprint. Discussion started: 13 November 2023

Geosci., 9, 433–437, https://doi.org/10.1038/ngeo2705, 2016a.

Wang, B., Knopf, D. A., China, S., Arey, B. W., Harder, T. H., Gilles, M. K., and Laskin, A.: Direct observation of ice nucleation events on individual atmospheric particles, Phys. Chem. Chem. Phys., 18, 29721–29731, https://doi.org/10.1039/C6CP05253C, 2016b.

Welti, A., Lüönd, F., Stetzer, O., and Lohmann, U.: Influence of particle size on the ice nucleating ability of mineral dusts, Atmos. Chem. Phys., 9, 6705–6715, https://doi.org/10.5194/acp-9-6705-2009, 2009.

Welti, A., Bigg, E. K., DeMott, P. J., Gong, X., Hartmann, M., Harvey, M., Henning, S., Herenz, P., Hill, T. C. J., Hornblow, B., Leck, C., Löffler, M., McCluskey, C. S., Rauker, A. M., Schmale, J., Tatzelt, C., van Pinxteren, M., and Stratmann, F.: Ship-based measurements of ice nuclei concentrations over the Arctic, Atlantic, Pacific and Southern oceans, Atmos. Chem. Phys., 20, 15191–15206, https://doi.org/10.5194/acp-20-15191-2020, 2020.

Wilson, T. W., Ladino, L. A., Alpert, P. A., Breckels, M. N., Brooks, I. M., Browse, J., Burrows, S. M., Carslaw, K. S., Huffman, J. A., Judd, C., Kilthau, W. P., Mason, R. H., McFiggans, G., Miller, L. A., Nájera, J. J., Polishchuk, E., Rae, S., Schiller, C. L., Si, M., Temprado, J. V., Whale, T. F., Wong, J. P. S., Wurl, O., Yakobi-Hancock, J. D., Abbatt, J. P. D., Aller, J. Y., Bertram, A. K., Knopf, D. A., and Murray, B. J.: A marine biogenic source of atmospheric ice-nucleating particles, Nature, 525, 234–238, https://doi.org/10.1038/nature14986, 2015.

Xiao, H.-S., Dong, J.-L., Wang, L.-Y., Zhao, L.-J., Wang, F., and Zhang, Y.-H.: Spatially resolved micro-Raman observation on the phase separation of effloresced sea salt droplets, Environ. Sci. Technol., 42, 8698–8702, https://doi.org/10.1021/es801181f, 2008.

Yakobi-Hancock, J. D., Ladino, L. A., and Abbatt, J. P. D.: Feldspar minerals as efficient deposition ice nuclei, Atmos. Chem. Phys., 13, 11175–11185, https://doi.org/10.5194/acp-13-11175-2013, 2013.

Yan, J., Jung, J., Zhang, M., Bianchi, F., Tham, Y. J., Xu, S., Lin, Q., Zhao, S., Li, L., and Chen, L.: Uptake selectivity of methanesulfonic acid (MSA) on fine particles over polynya regions of the Ross Sea, Antarctica, Atmos. Chem. Phys., 20, 3259–3271, https://doi.org/10.5194/acp-20-3259-2020, 2020.

Zhou, M. Y., Yang, S. J., Parungo, F. P., and Harris, J. M.: Chemistry of marine aerosols over the western Pacific Ocean, J. Geophys. Res., 95, 1779, https://doi.org/10.1029/JD095iD02p01779, 1990.